Journal of Sound and Vibration 572 (2024) 118157

Contents lists available at ScienceDirect

Journal of Sound and Vibration

journal homepage: www.elsevier.com/locate/jsvi

Smart controllable wave dispersion in acoustic metamaterials using magnetorheological elastomers

Vyacheslav N. Gorshkov [a,b], Vladyslav O. Kolupaiev [a], Gernot K. Boiger [c], Navid Mehreganian [b,d], Pooya Sareh [b,e], Arash S . Fallah [c,f,g,*]

[a] Department of Physics, Igor Sikorsky Kyiv Polytechnic Institute, National Technical University of Ukraine, 37 Prospect Peremogy, Kiev 03056, Ukraine
[b] Creative Design Engineering Lab (Cdel), Department of Mechanical and Aerospace Engineering, School of Engineering, University of Liverpool, Liverpool L69 3GH, UK
[c] Institute of Computational Physics, Zürich University of Applied Sciences, Wildbachstrasse 21, Winterthur 8400, Switzerland
[d] Department of Civil and Environmental Engineering, Imperial College London, Skempton Building, South Kensington Campus, London SW7 2AZ, UK
[e] School of Engineering, Newcastle University, Newcastle upon Tyne, NE1 7RU, UK
[f] Department of Mechanical, Electronic and Chemical Engineering, OsloMet, Pilestredet 35, Oslo 0166, Norway
[g] Department of Aeronautics, Imperial College London, City and Guilds Building, South Kensington Campus, London SW7 2AZ, UK

ARTICLE INFO

Keywords:
Active filtering
Acoustic metamaterial
Magnetorheological elastomer
Band structure
Multi-particle core
Core-shell structure

ABSTRACT

The success in the flexible design of smart acoustic metamaterials is crucially contingent upon the degree of control over the parameters that uniquely define the spectrum of band structure and morphology of dispersion surfaces. In this work, we have studied the driving physical mechanisms, the control of which makes possible operating, in real-time, on the set of band gaps formed in 3D metamaterials based on magneto elastomers. In such acoustic structures, the stiffness of the medium in which unit cells are immersed, as well as the stiffness of the shells surrounding multi-particle cores depend on the induction, $B(t)$, of an external magnetic field. The results obtained are systematized through the qualitative analysis of diverse scenarios for the evolution of the frequency characteristics of the metamaterial and summarized in the following complete physical picture of their dynamics. Variation of the stiffness of the medium/shells changes the wavelength of the shell's surface waves at characteristic frequencies of the core vibrations and, as a result, the level of coupling between the vibration modes of the flexible shells and cores. Consequently, with an increase/decrease in the stiffnesses of the shells/medium, the dispersion surfaces of the entire acoustic system shift up/down along the frequency axis with noticeably different 'mobilities' that reversibly lead either to the formation of the band gaps in initially dense frequency spectrum or to the transformation of the band gaps formed into pass bands. The tuning of the set of dispersion surfaces depending on the range of changes in the magnetic field induction can be carried out in dynamic, quasi-stationary, and over-critical regimes when some of the dispersion surfaces degenerate into planes. In anisotropic metamaterials, simultaneously with creating full band gaps, it is possible to create tunable directional band gaps with adjustable frequency and angular widths. The results obtained, within the framework of the idealized discrete mass-spring model, are in good agreement with the data presented in the available experimental works and can be useful in the design of acoustic systems with desirable properties.

* Corresponding author.
E-mail addresses: arashsol@oslomet.no, as3@imperial.ac.uk (A. S . Fallah).

https://doi.org/10.1016/j.jsv.2023.118157
Received 12 May 2023; Received in revised form 10 October 2023; Accepted 6 November 2023
Available online 16 November 2023

1. Introduction

In recent years, a lot of attention has been paid to the study of the physical properties of acoustic metamaterials (AMM) and phononic crystals (PC), which are artificially designed smart materials created to own capabilities and potentials beyond those of natural materials [1–5]. Scientific advances in this area have greatly expanded our ability to control sound waves in the process of their transmission, reflection, refraction, absorption, diffraction, and attenuation. Analogous to electromagnetic/optical metamaterials [6], the emergence of properties or phenomena as negative refractive index of the medium [7,8], negative stiffness [9–12], negative Poisson's ratio [13–16], acoustic cloaking [17,18], and acoustic superlensing [19,20] are realized in acoustics.

One of the important properties of PCs and AMMs is their ability to block the passage of sound waves of certain frequency ranges in such media, i.e. to create bandgaps. In PCs, bandgaps are formed as a result of wave interference after Bragg scattering of the incident acoustic waves [21–25]. Since in this case, the wavelengths are of the same order of magnitude as a directional lattice constant i.e. the directional spatial period of the structure, the created stopband corresponds to relatively high frequencies. In AMMs, the incident acoustic wave interacts with local resonators/unit cells of diverse types e.g. Helmholtz resonators [26–28], membrane-type structures [29,30], multi-resonators of mass-in-mass type [31,32], fractal/pseudo-fractal [33–35], chiral [36,37], or labyrinthine [38–40] microstructures. The edges of the bandgaps formed are determined only by the resonant frequencies of unit cells. The corresponding sound wavelengths can thus significantly exceed the lattice constant so that bandgaps form in a relatively low-frequency range which is important for practical implementations such as noise reduction [41], underwater detection [42], or medical imaging [43].

In the modern physics of acoustic metamaterials, one of the important problems is the development of methods for generating a controlled spectrum of propagating acoustic waves [23,44–48]. One solution may be found and implemented through the successful selection of design parameters and proper assignments made in predefined arrangements of geometry, topology, and mass and stiffness distributions within the unit cell of metamaterials. This way, the goal of the creation of specific bandgaps may be achieved – this is the so-called 'passive' method which does not allow changing the bandgap parameters in real-time.

Despite the useful properties of the aforementioned designs, more flexible real-time control is desirable. This possibility may be realized through changing the elastic properties of metamaterial elements by various external physical factors. Authors of the work [49] used piezoelectric springs in the one-dimensional periodic structure to tune various types of band gaps with electrical stimuli, which caused a change in the elastic modulus of resonators and their natural frequencies. Drawing on the mechanical properties of an origami pattern known as the Miura-ori [50–52], the tunability of complete bandgaps or partial bandgaps in specific directions is investigated in a proposed novel perforated Miura-ori phononic structure when the morphology of its unit cells changes [53]. On the base of the three-dimensional printed hollow sphere lattice metamaterials, tunable phononic bandgaps magnified by 37.5 % are realized in work [54], in which the bandgap control is carried out through the reversible temperature-dependent stiffness of the glassy polymer and discontinuity of stable thermal field in the lattice structure.

In this work, we consider the possibility of 'active' control of band gap parameters when the controlling factor is an external magnetic field, which changes the elasticity of unit cells through magnetic induction, B, and, accordingly, the frequency characteristics of the AMM as a whole. Magnetic field-sensitive AMM elements are comprised of artificial materials i.e. Magnetorheological Elastomers (MRE) [55,56].

MREs are the result of the solidification of a nonmagnetic polymer filled with micro-sized magnetic particles and other additives. The type of filler [57–60], particle size [58], and their arrangement in the matrix [59,61] determine the level of sensitivity of this particulate composite to an external magnetic field. In particular, a significant increase in the moduli of elasticity of the material in sufficiently moderate magnetic fields of the order of 50∼600 mT. For instance, in a magnetic field with an induction of 500 mT, elastomers containing carbonyl iron particles showed an increase in the elastic modulus by a factor of 277 [62,63]. Such changes occur rapidly (in a time range counting up to several milliseconds [64]) and reversibly [65,66]. Since the magnetic field is a convenient control factor, the use of MREs in technology as intelligent materials [67,68] is very promising in numerous engineering applications such as the design of actuators and sensors [69–71], vibration dampers [72,73], and adaptive stiffness devices [55,74].

The possibilities of controlling the spectrum of propagating acoustic waves in 2D-AMMs were studied in [75–80], in which AMM unit cells had various shapes and formed various structures. In [81], a metamaterial plate incorporating magnetorheological elastomers and multiple gradient resonators was investigated, in which an adaptive magnetic field adjustment mechanism works to alter the elastic modulus of the MRE in order to modulate the local resonance bandgap. Wang et al. [82] studied a semi-active graded MRE metamaterial sandwich beam with real-time tunable graded stiffness. The results show that the width of the band gap in the proposed system can be increased by grading the stiffness of the MRE in an ascending order. The change in the width and position of the band gap for transverse waves in magnetically active laminates was demonstrated in [83].

As far as dimensions of the space are concerned, the unit cells in two-dimensional [75,84] and three-dimensional [85] metamaterials have a topologically similar structure. The cores of the unit cells (flat cylinders [75], cubes, or balls [85]) were covered with MRE-shells. The unit cells formed were ordered either on a flat plate from the same MRE [75] or in an epoxy matrix [85] without direct contact between the nearest cells. In both cases, with an increase in the induction of the external magnetic field, the bandgap edges gradually move to high frequency, and the band gap width becomes wider. The analogical bandgap transformation is observed in work [84]. Note that for 3D-AMM [85] the results were obtained using the finite element method.

The peculiarity of the studies conducted is that the band gaps have already been formed in the initial state i.e. in the absence of a magnetic field (the induction of external magnetic field $B = 0$). When they shifted and expanded with increasing magnetic field magnitude, a significant part of the frequency spectrum remained common to the initial and "movable" band gaps. Examples of regimes in which the band gap arose in the initial transmission spectrum with increasing magnetic field magnitude and only transformed

afterward are not given in the aforementioned works.

In our work, within the framework of the idealized discrete spring-mass model, we explore physical mechanisms to extend the possibilities of active control through judicious alteration of frequency parameters of 3D-AMMs based on MREs. The structure of the metamaterial subject to this investigation, which is described in detail in the sequel, represents a generalized version of the metamaterial in the form of an ordered lattice of multivibrators/cores embedded in a cellular elastic medium - the substratum MRE-skeleton that is sensitive/responsive to the induction of a magnetic field. Variations in the external magnetic field change the coupling between the vibrational modes of the cores and the skeleton, which leads to a variety of scenarios for the formation of complete or partial bandgaps in specific directions in the initially continuous transmission spectrum. The physical mechanisms responsible for both the appearance of bandgaps and for their further evolution are analyzed in detail qualitatively and illustrated graphically. The main attention is paid to the search for regularities in dependence of functionality on ratios of cores and skeleton parameters for controlling the acoustic properties of the system from the creation of the bandgaps to their quasi-steady state with increasing magnitude of the magnetic field induction.

The present paper is organized in the following sections. In Section 2, we analyze the basis for the physical conception of band gap formation and the effects of nonlocal interactions. In Section 3 the representative discrete-parameter model i.e. the 3D mass-spring model of the acoustic metamaterial is adopted and the relevant dispersion equations are derived. A multitude of scenarios for band gap dynamics control for a number of unit cell constructions is discussed in Section 4 including the formation of directional band gaps in the anisotropic metamaterial. In Section 5 a short final review of the results obtained is presented.

2. Physical conception of bandgap formation and effects of nonlocal interactions

In this section, we analyze the physical conceptions of controlling the structure of the formed band gaps by an external magnetic field based on the proposed spring-mass model. Unit cells with cubic symmetry of the internal structure (one of the variants of such a cell is shown in Fig. 1(a)) consist of a multi-particle core (red spheres) and a multi-particle shell surrounding the nucleus (blue spheres). These directly interact with each other's unit cells and, in turn, form a cubic 3D lattice of an acoustic metamaterial. One of the possible cross-sections of the medium formed this way is shown in Fig. 1(b). Each one of the particles (red/blue sphere) interacts with 26 nearest particles through springs connecting them. The stiffness of the springs, κ, inside the cells (marked olive in Fig. 1(b)) does not depend on the induction of the external magnetic field. The stiffness of the springs connecting the cells, χ, and the stiffness of the springs, η, between the particles of the single shell (blue thin and thick lines in Fig. 1(b), respectively) depend on the magnetic field and in most cases are assumed equal ($\eta = \chi$). But, at times, and to demonstrate the relationship between various physical factors that determine the features of the frequency characteristics of acoustic waves, processes are considered in which these parameters are different i.e., $\eta \neq \chi$.

The main physical concepts of real-time active band gap control can be most clearly shown using discrete AMM models. It is for this reason that the structural form used in our research was chosen as shown in Fig. 1 accounting for a different number of particles in the core and, respectively, in the surrounding shell.

For an initial qualitative analysis, let us scrutinize the formation of a band gap in a one-dimensional chain of simple (single) vibrators (Fig. 2A(a)). Obviously, in the absence of an external elastic medium (external springs of stiffness χ), the free vibrator oscillates with a frequency $\omega_f^2 = 2\kappa/M^*$, where M^* is the reduced mass (of the two-body problem) derived as $M^* = Mm/(M+m)$, where M and m are the masses of the shell and the core, respectively. In the acoustic chain (Fig. 2A(a)) each vibrator is subject to external perturbations from the surrounding elastic medium. When an acoustic wave of wavelength λ propagates in the chain, springs with an effective stiffness $\chi^*(\lambda) \neq \chi$ act on the vibrator shell, since this effective stiffness depends on the relative displacements of neighboring shells, i.e. on the wavelength λ. The necessity of bandgap formation in the chain under consideration can be easily deduced from the equations of

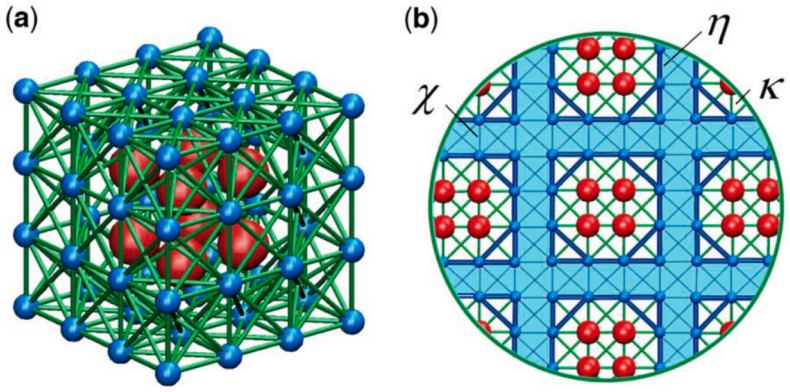

Fig. 1. Morphology of the acoustic metamaterial under consideration in the spring-mass model. Configuration (**a**) presents the typical structure of the elementary cell. Red particles-spheres represent the core, blue particles - the shell. Configuration (**b**) depicts a section of the acoustic medium by a plane passing through the red particles of the cores.

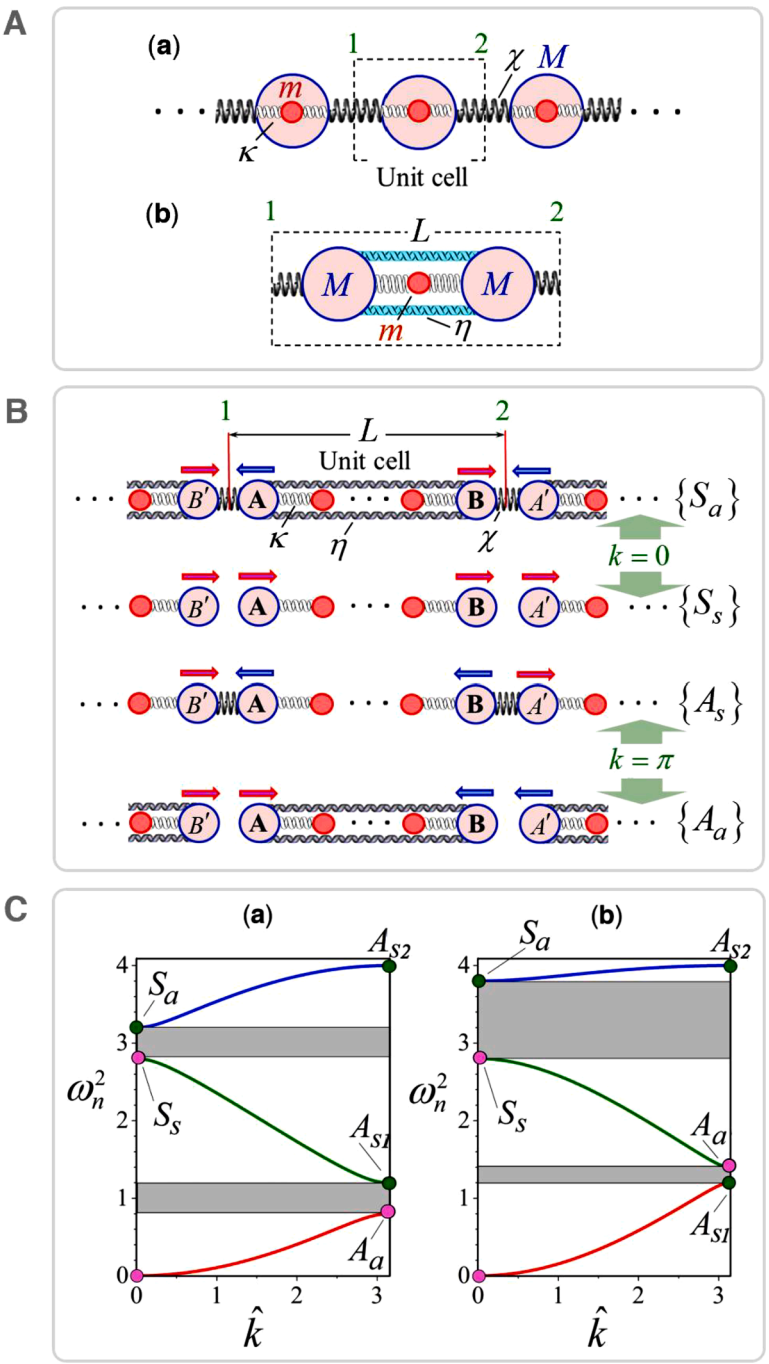

Fig. 2. Acoustic waves in one-dimensional elastic chains. (**A**) Part (**a**) shows the chain structure with simple mass-in-mass resonators at its nodes, and part (**b**) depicts the unit cell of the chain in the case when the elements of the composite shell of the resonator are connected by a nonlocal interaction. (**B**) Classification of vibration modes of elementary cells in the center of the Brillouin zone and on its boundary according to different types of symmetry. Springs that do not deform when a given type of vibration mode is excited are not shown in the corresponding graphical representation of the vibration pattern of that type. (**C**) Frequency branches of oscillations, $\{\omega_n^2(\hat{k})\}$, in a one-dimensional chain with elementary cells, the structure of which is shown in Fig. 2A(b); $m = 1$, $M = 1.25$, $\chi = 1.5$ ($\Omega^2 = \frac{\chi}{M} = 1.2$). (**a**) $\eta = 0$, and (**b**) $\eta = 0.15$ ($\Omega_{nl}^2 = \frac{\eta}{M} = 0.12$).

motion for the core and the shell as follows:

$$M\ddot{x}_e = \kappa\delta x_i - \chi^* x_e \text{ and } m\ddot{x}_i = -\kappa\delta x_i. \tag{1}$$

Here x_i and x_e are the displacements of the core and the shell, respectively, and $\delta x_i = x_i - x_e$ is the displacement of the core relative

to the shell. For harmonic in-phase solutions, $x_e = x_{eo}e^{i\omega t}$, $x_i = x_{io}e^{i\omega t}$, we obtain two representations for δx_{i0}:

$$\delta x_{i0} = \frac{\omega^2}{\omega_0^2 - \omega^2} x_{e0} \text{ and } \delta x_{i0} = \frac{\chi^*(\lambda)}{M} \frac{1}{\omega_f^2 - \omega^2} x_{e0}, \tag{2}$$

where $\omega_0^2 = 2\kappa/m$ ($\omega_0^2 < \omega_f^2$).

The requirement of the same sign for the coefficients of x_{e0} on the right-hand side of equations (2) does not allow propagation of waves of frequencies in the interval expressed in the inequality of relation (3).

$$\omega_0^2 < \omega^2 < \omega_f^2. \tag{3}$$

The lower and upper branches of allowable frequencies, $\omega_{1,2}^2 = \omega_{1,2}^2(\lambda)$, are determined by the dispersion equation:

$$\frac{\left(\omega_f^2 - \omega^2\right)\omega^2}{\omega_0^2 - \omega^2} = \frac{\chi^*(\lambda)}{M}. \tag{4}$$

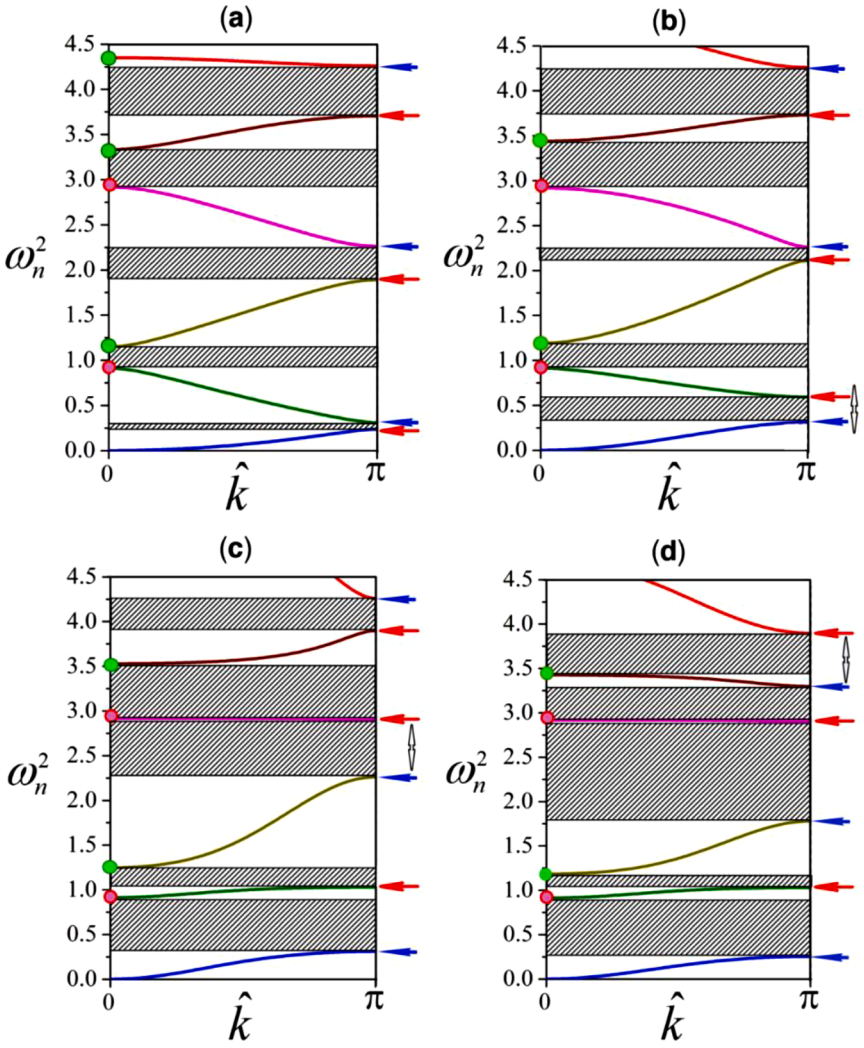

Fig. 3. Dynamics of the sets of characteristic points and band gaps with variation in the stiffness of the environment, χ, and non-local interaction, η, in the chain presented in Fig. 2(B). The number of red particles in the core is 4 and the mass of each of them is $m = 1$. The mass of each of the shell particles is $M = 1.2$ and the stiffness of the internal springs is $\kappa = 1$. Red circles mark frozen frequencies from the set of modes $\{S_s\}$, green circles - mobile modes from the set $\{S_a\}$, horizontal red arrows - are sensitive to variations in η modes from the set $\{A_a\}$, blue arrows - sensitive to changes in χ modes from the set $\{A_s\}$. Vertical arrows mark the switching between modes of different sets. Configuration (**a**) - frequency branches $\omega_n^2(\hat{k})$ at $\chi = 1.8$ ($\Omega^2 = \frac{\chi}{M} = 1.5$), $\Omega_{nl}^2 = \frac{\eta}{M} = 0$; (**b**)- $\Omega^2 = 1.5$, $\Omega_{nl}^2 = 0.15$; (**c**)- $\Omega^2 = 1.5$, $\Omega_{nl}^2 = 0.5$; (**d**) -parameter Ω_{nl}^2 remained the same as for configuration (c), $\Omega_{nl}^2 = 0.5$, but the value of Ω^2 was reduced: $\Omega^2 = 0.75$.

The result obtained shows that by varying the stiffness of the external springs in any way (including through induction of a magnetic field) it is impossible to change the characteristics of the formed bandgap. At the same time, it is technically difficult to influence the elastic characteristics, κ, of the internal structure of vibrators by a magnetic field, although such a possibility, in our opinion, was realized in [81]. In this work, the design of the unit cells mimics that of a mass-in-mass resonator, for which the upper edge of the bandgap, $\omega_f^2 = 2\kappa(B)/M^*$, rises faster than its lower boundary, $\omega_0^2 = 2\kappa(B)/m$, while both vary linearly with increasing stiffness $\kappa(B)$. A more realistic option for tuned bandgap formation is to change the elastic properties of the shells, which are not rigid and are themselves multi-particle vibrators.

In the simplest case, such a shell can be idealized as being composed of two parts with the inclusion of a non-local interaction between them along an integral chain, as shown in Figs. 2A(b) and 2(B) (a shell of two parts A and B encloses a many-particle nucleus in an arbitrary case). In the sequel, we shall discuss those properties of such one-dimensional chains that are important for the analysis of similar but more complex systems.

The set of frequency branches, $\omega_n^2 = \omega_n^2(\widehat{k})$ ($\widehat{k}$ being the dimensionless wave vector $\widehat{k} = 2\pi L/\lambda$, where L is the length of the unit cell) starts at the set of points, $\{\omega_n^2(\widehat{k}=0)\}$, on the frequency axis at $\widehat{k}=0$ and ends at the corresponding points of the set $\{\omega_n^2(\widehat{k}=\pi)\}$ (on the boundary of the Brillouin zone) as depicted in Figs. 2(C) and 3. These points react differently to changes in the stiffness of external springs, χ, and nonlocal bonds, η, induced by the magnetic field. This can be easily verified by analyzing the morphology of the different types of possible vibration modes at the center of the Brillouin zone and on its boundary (see Fig. 2(B)). It can be seen that the set of modes symmetric about the center of the unit cell, $\{S_s\}$, do not respond at all to changes in the values of χ and η, since these springs do not deform on exciting waves of the specific type. Such modes are 'frozen' in a certain sense while the 'mobile' set $\{S_a\}$, conversely, reacts to changes in each of the stiffnesses χ and η. At the boundary of the Brillouin zone, the sets $\{A_s\}$ and $\{A_a\}$ react only to changes in the stiffness χ in the first case and the stiffness η in the second. Note that the sets of frequencies $\{S_s\}$ and $\{A_a\}$ represent the eigenfrequencies of an isolated unit cell i.e. without taking into account the effect of external springs on it. The frequency sets $\{S_a\}$ and $\{A_s\}$, on the other hand, correspond to eigenfrequencies of an 'open' primitive cell with fixed boundaries (see points 1 and 2 in Fig. 2(B)). External springs (formally shortened) act on the shell of such a cell to the left and the right with effective stiffness 2χ.

The manifestation within the sets $\{\omega_n^2(\widehat{k}=0)\}$ and $\{\omega_n^2(\widehat{k}=\pi)\}$ of different mobility of characteristic frequencies with changes in the elasticity parameters of the external medium and shells is visible in the data presented in Figs. 2(C) and 3.

It should be noted that for $M \neq m$, band gaps can also form in the absence of nonlocal interactions (Figs. 2(C)-(a)), while with nonlocal interaction included, they form even if the masses were equal i.e., $M = m$. However, in the general case, the result of the inclusion of nonlocal interactions can be a reduction in the number of band gaps. For example, if for the data presented in Figs. 2(C)-(a), we increase η to the value of $\eta = 0.095$, then only the frequencies from sets A_a and S_a will respond/increase, moreover, the frequency of A_a will coincide with the frequency of A_{s1} and the lower band gap will disappear (converts to passband). With a further increase in the parameter η, switching occurs between the two lower frequency branches at the boundary of the Brillouin zone (Figs. 2(C)-(b)) with the formation of a new bandgap above the A_{s1} mode, which is stationary in this case. An increase in the number of particles in the cores increases the number of frequency branches $\omega_n^2(\widehat{k})$, the number of characteristic points, and, accordingly, the number of band gaps (See Fig. 3). The movement of characteristic points along the numerical axis with variation in the elasticity of the shells of elementary cells and their environment is accompanied by several shifts between frequency surfaces both at the border of the Brillouin zone (See Fig. 3) and at its center (See Video file '1D-Bandgap Dynamics' in Supplementary Materials).

For the 3D metamaterials considered below, the general structure of which is shown in Fig. 1, the set of oscillation modes at $\widehat{k}=0$ and singular points on the boundary of the Brillouin zone (see Fig. 4) also have different mobilities with changes in stiffness parameters $\chi(B)$ and $\eta(B)$ (B is the norm of the external magnetic field induction) causing inhomogeneous movement of the wave surfaces in 4D-

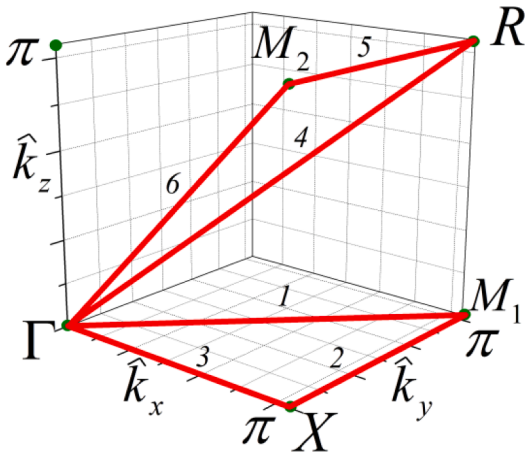

Fig. 4. The trajectory in $\widehat{k}-$ space for calculations of frequency-branches, $\omega^2 = \omega_m^2(\widehat{k})$, to study their morphology over the irreducible Brillouin zone i.e. the region $0 \leq \widehat{k}_{x,y,z} \leq \pi$.

space $\omega^2 = \omega_n^2(\widehat{\boldsymbol{k}})$, $n = 1, 2, 3, \ldots, 3N$, where N is the number of mass particles (material points) in a unit cell. Thus, it is this inhomogeneity in the mobility of wave surfaces that is the main factor for the controlled effective mixing/switching of these surfaces and the corresponding change in the positions and width of the band gaps up to their complete disappearance. Moreover, in anisotropic structures, the disappearance of band gaps for waves across the axis of anisotropy can be accompanied by their formation for waves propagating along this axis.

3. Parameters of 3D mass-spring model and construction of the dispersion equations

In the general case, the core of the unit cell (see Fig. 1) contains N_{core} particles: $N_{core} = n^3$, $n = 1,2,3\ldots$ The core is surrounded by a shell, which consists of $N_{shell} = (n+2)^3 - n^3$ particles. The shortest distance between neighboring particles is normalized to 1. The stiffness of the horizontal/vertical (i.e., the shortest) springs connecting the core particles and the shell particles is equal to κ. The stiffness of the horizontal/vertical springs acting between the shell particles inside the unit cell is equal to η. A similar value of χ holds for springs connecting neighboring unit cells. It is assumed that a linear spring captures interaction effects accurately enough and its potential is of logarithmic form of the initial length. Thus, the numerical model takes into account the inversely proportional dependence of the spring stiffness on their length. For example, 6 springs with stiffness κ, 12 springs with stiffness $\kappa/\sqrt{2}$, and 8 springs with stiffness $\kappa/\sqrt{3}$ act on a particle of the core. The general form of the dispersion equation is therefore:

$$\boldsymbol{A}\boldsymbol{u} = \omega^2\boldsymbol{u}, \tag{5}$$

where $\boldsymbol{u}$ signifies the displacement vector i.e. the transposed column vector of $\boldsymbol{u}^{\boldsymbol{T}} = (\boldsymbol{x}^{\boldsymbol{T}}, \boldsymbol{y}^{\boldsymbol{T}}, \boldsymbol{z}^{\boldsymbol{T}})$, where, $\boldsymbol{x}^{\boldsymbol{T}} = (x_1, x_2, x_3, \ldots, x_N)$, $\boldsymbol{y}^{\boldsymbol{T}} = (y_1, y_2, y_3, \ldots, y_N)$ and $\boldsymbol{z}^{\boldsymbol{T}} = (z_1, z_2, z_3, \ldots, z_N)$, with N being the total number of particles in the unit cell as:

$$N = N_{core} + N_{shell}. \tag{6}$$

The sets $\{x_i\}, \{y_i\}, \{z_i\}$ represent the displacements of the main particles (particles lying inside the single unit cell). Matrix $\boldsymbol{A}$ is a square matrix of dimension $3N$ and is composed of the coefficients of the equations of motion for these particles. When constructing these equations for the shell particles, the displacements of particles outside the main unit cell must be considered. These displacements are not independent but are connected by a linear relationship with the displacements of particles in the main cell. Each of the 'external'/equivalent particles has a primary particle inside the shell of the main cell. The vector connecting the primary particle with the equivalent particle must be equal to one of the lattice translation vectors of the form:

$$\boldsymbol{a} = l_x \cdot \boldsymbol{a}_{\boldsymbol{x}} + l_y \cdot \boldsymbol{a}_{\boldsymbol{y}} + l_z \cdot \boldsymbol{a}_{\boldsymbol{z}}, \tag{7}$$

where $|\boldsymbol{a}_{\boldsymbol{x}}| = |\boldsymbol{a}_{\boldsymbol{y}}| = |\boldsymbol{a}_{\boldsymbol{z}}| = \mathscr{L} = (n+2), l_x, l_y, l_z$ -are integers, which can take the values $-1,\ 0,\ +1$, and $\mathscr{L}$ is lattice constant of the constructed cubic structure. The number of the equivalent particles, $(n+4)^3 - (n+2)^3$, is greater than the number of particles in the shell, N_{shell}. As a result, one, three, and even seven equivalent particles can correspond to one primary particle.

When a wave propagates in a metamaterial, the displacement, $\boldsymbol{u}_j$, of the equivalent particle with index j and displacements, $\boldsymbol{u}_i$, of the main particles with index i are interconnected by Bloch's theorem (also known as Floquet-Bloch's principle) as:

$$\boldsymbol{u}_j = \boldsymbol{u}_i \cdot \exp(i\boldsymbol{k}\boldsymbol{a}_{ij}) \tag{8}$$

where $\boldsymbol{k}$ ($k = 2\pi/\lambda$) is the wave vector of the acoustic wave with the wavelength λ, $\boldsymbol{a}_{ij}$ is the vector that connects these particles (see Eq. (7)). In sequel, we will operate with the dimensionless wave vector $\widehat{k} = 2\pi\mathscr{L}/\lambda$.

For small-amplitude harmonic vibration of particle i, i.e. its small oscillations around the equilibrium position, $\boldsymbol{u}_i = \boldsymbol{u}_{i0}\exp(i\omega t)$, the equations of motion, $m_i\ddot{\boldsymbol{u}}_i = \boldsymbol{f}_i$ ($i = 1, 2, 3, \ldots, N$) take the following form:

$$-\boldsymbol{u}_{i0}\omega^2 = \sum_{j=1}^{26} \boldsymbol{e}_j \left(\frac{\kappa_{ij}}{m_i}\right)\left(\boldsymbol{e}_j \cdot \left(\boldsymbol{u}_{j0} - \boldsymbol{u}_{i0}\right)\right). \tag{9}$$

The summation in Eq. (9) is carried out in 26 directions from the central, i-th, particle to the lattice particles surrounding it and the vectors $\{\boldsymbol{e}_j\}$ are unit vectors defined as $\boldsymbol{e}_j = \boldsymbol{a}_{ij}/a_{ij}$, oriented along these directions, κ_{ij} – the stiffness coefficients of the corresponding springs, $\boldsymbol{u}_{i0,j0}$ – the amplitudes of oscillations of the particles, which are in general complex, m_i – the mass of the central particle. The dependence of matrix $\boldsymbol{A}$ (i.e., its entries formed by the coefficients of N equations of the form Eq. (9)) on the dimensionless wave vector, $\widehat{k} = 2\pi\mathscr{L}/\lambda$ in Eq. (8) is a consequence of applying Bloch's theorem to deviations at auxiliary lattice nodes.

Since the size of matrix $\boldsymbol{A}$ is equal to $3N \times 3N$, the solution of Eq. (5) entails a set of dispersion surfaces $\omega^2 = \omega_m^2(\widehat{\boldsymbol{k}})$, $m = 1, 2, 3, \ldots, 3N$ in 4-dimensional space. Through graphical presentation and physical analyses of this set, we calculate sections of these surfaces along a trajectory in the first Brillouin zone (see. Fig. 4), taking into account the cubic symmetry of the system under consideration.

The intelligent computational procedure that forms the elements of matrix $\boldsymbol{A}$ based on Eqs. (9) is embedded in an optimized computer code that rapidly calculates the eigenfrequencies of matrix $\boldsymbol{A}$ at 1200 points evenly spaced on the $\widehat{\boldsymbol{k}}$ – trajectory shown in Fig. 4.

Concerning the parameters of the system under consideration, we assume the unit of masses is the mass of the red core particle, m, and the unit of stiffnesses is the stiffness κ (see Fig. 1). Thus, the independent parameters are the mass of the blue shell-particles, m_{shell},

stiffness η and stiffness χ (see the description of Fig. 1 above). Eq. (5) is divided by the value κ/m which reduces it to a dimensionless form.

4. Intermixing of the dispersion surfaces in the 3D-bandgap dynamics

In this section, we shall consider the formation and dynamics of band gaps in systems with different numbers of particles in their cores, including the cases when the cores are anisotropic (elongated along one of the main axes). When choosing the parameters of the shells and the environment, the following physical factors should be considered. The first of them is related to the fact that the formation of a band gap over the range of acoustic vibrations has a significant deal in common with the splitting of the energy levels of a simple mass-in-mass vibrator, even though in the cases under consideration the shells are flexible. At low frequencies, one way or another, oscillations of a many-particle core can be considered, with a rather good approximation, as the motion of a single entity as the whole for estimating the parameters of the emerging band gap. According to Eq. (3), the band gap, $\Delta\omega^2 = \omega^2_{up} - \omega^2_{down}$ (where ω^2_{up} and ω^2_{down} present upper and down edges of the bandgap respectively) is of the order of the difference between the frequency of an isolated vibrator, $\omega^2_{up} \approx \omega^2_f$, and the frequency of a vibrator with a fixed shell, $\omega^2_{down} \approx \omega^2_0$. Thus, up to some extent,

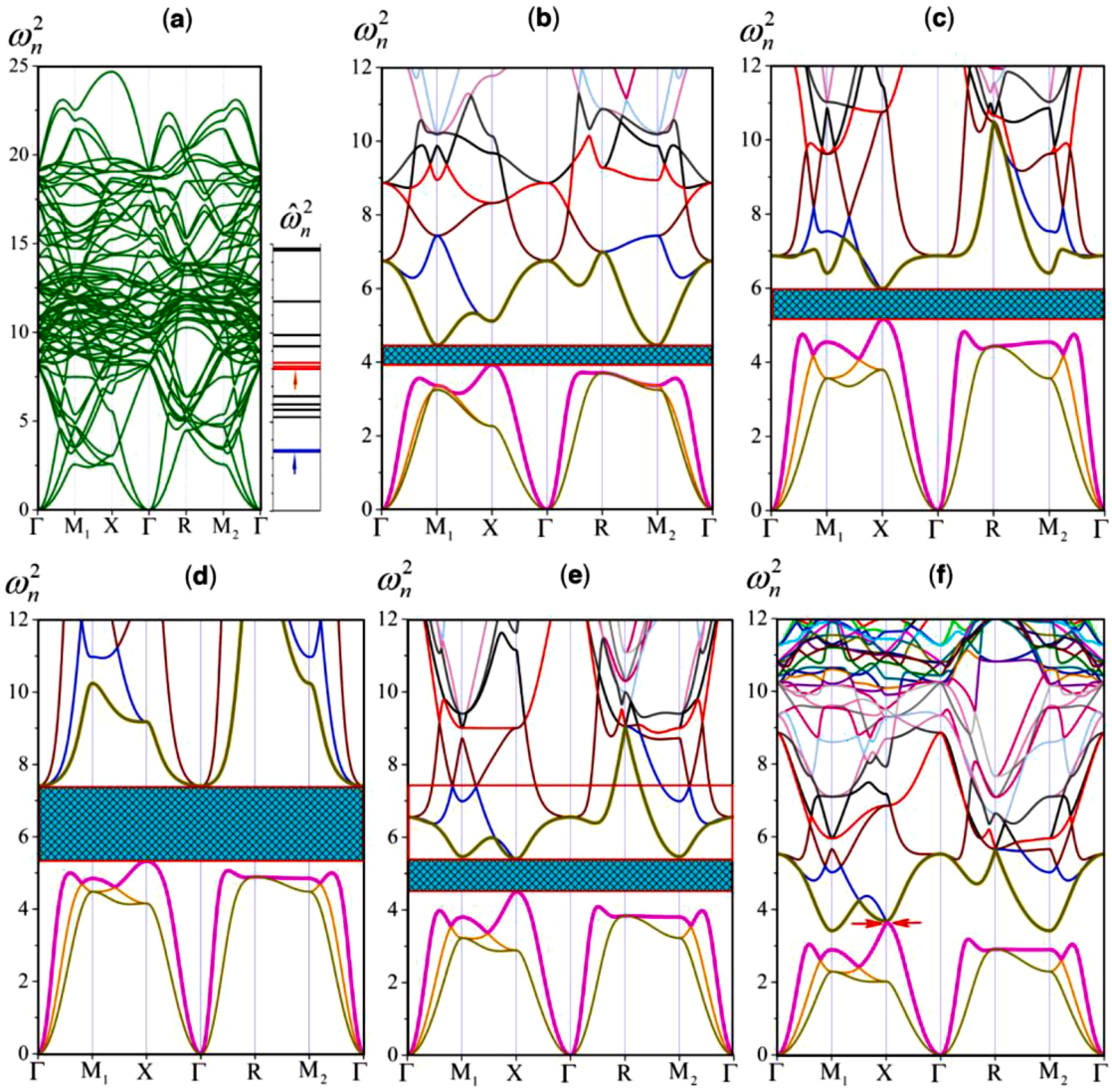

Fig. 5. Frequency characteristics of a 3D metamaterial with a single-particle core in an elementary cell. (**a**) Dependences $\omega_n^2(\boldsymbol{k})$ for the metamaterial skeleton along the trajectory shown in Fig. 4(a), $\eta = \chi = 0.25$, and $m_{shell} = 0.125$. On the right is the eigenfrequency spectrum, $\hat{\omega}_n^2$, of an isolated cell ($\eta = 0.75$). (**b**) Dependences $\omega_n^2(\boldsymbol{k})$ at $\chi = 0.25$ and $\eta = 0.75$ for the entire metamaterial. (**c**) $\chi = 0.75$ and $\eta = 0.25$. Configurations (**d**), (**e**), and (**f**) demonstrate the band gap dynamics with a gradual decrease in stiffnesses: $\eta = \chi = 0.75$, 0.40, and 0.25, respectively.

$$\Delta\omega^2 \approx \omega_f^2 - \omega_0^2. \tag{10}$$

So, a practical conclusion is that the difference in the masses of the shell, M_{shell}, and the core, M_{core}, should not be significant for creation of the noticeable relative bandgap:

$$\Delta\omega^2 \Big/ \omega_f^2 = (1 + M_{shell}/M_{core})^{-1}. \tag{11}$$

The second of the necessary physical factors in our model (Fig. 1), is the adequately strong coupling between the vibration modes of the unit cell and the vibration modes of the 'skeleton' of the acoustic system (recall that so-called 'skeleton' is the remnant lattice ensued after the extraction of the cores). This coupling should ensure that a gap appears in the initially continuous spectrum of the whole system as the magnitude of the magnetic field induction increases in order to provide a sufficiently strong splitting of the skeleton wave surfaces, $\omega_m^2(\widehat{\boldsymbol{k}})$, at the points of its intersection with the linear spectrum of the unit cell. These conditions are met in the systems discussed below. In particular, the freedom in the choice of values for elastic parameters χ and η provides a wider frequency range for the skeleton than for isolated cell modes (see, for example, Fig. 5(a)).

4.1. The dispersion-surface dynamics in single-resonator metamaterials

Obviously, in the case of multiparticle shells of unit cells, the estimation of the bandgap width from relation (10) will be most accurate at high values of the stiffnesses η and χ. The dependence of the bandgap upper and lower limits on the magnitude of the magnetic field induction, $\omega_{up}^2(B)$ and $\omega_{down}^2(B)$ saturates and these tend to their limiting values as the skeleton system increasingly manifests itself as a unified whole. In our opinion, it is this saturation mode that corresponds to the experiments conducted by researchers [75] (massive copper discs surrounded by magneto elastomer shells). In these experiments, the band gap, which already exists at $\boldsymbol{B} = 0$, only slightly shifted and broadened with an increase in the external magnetic field's intensity. This means that in the initial state the stiffness of the skeleton was high enough to form band gaps in the aforementioned 'classical' way.

In the sequel, we shall show how more noticeable variations in the parameters of the band gaps (width and position in the frequency spectrum) can be achieved by reducing the initial rigidity of the shells, which is quite feasible, and will qualitatively analyze the dynamics of the bandgap throughout different stages of its evolution.

The data in Fig. 5 give a representation of the processes that reversibly occur in the acoustic system, both from the initial formation of the band gap to its most developed phase/width with an increase in the stiffness of the homogeneous medium surrounding the cores ($\eta = \chi$) and in the reverse direction of the sequence. The video 'Initial_Stage.mp4' in Supplementary Materials shows, in detail, an increase in the rigidity of the external environment leads to a line spectrum of isolated cells transforming into a continuous spectrum of the whole metamaterial in which a band gap arises. It is its gradual disappearance during the reverse course of the process that is shortly presented in the configuration sequence (d)-(e)-(f) in Fig. 5.

We note below that the result of the configuration in Fig. 5(d) corresponds well with the qualitative assessment expounded above. With a fixed shell, a single-particle core ($M_{core} = m = 1$) is under the influence of 26 springs with an effective isotropic stiffness, $\mathscr{K}^*$. According to the Eq. (9):

$$\mathscr{K}^* = 2 + 8\Big/\left(2\sqrt{2}\right) + 8\Big/\left(3\sqrt{3}\right) \approx 6.37,\ \omega_0^2 = \frac{\mathscr{K}^*}{M_{core}} \approx 6.37. \tag{12}$$

Thus, for given masses of the core, $M_{core} = 1$, and shell, $M_{shell} = 3.25$ (the corresponding reduced mass $M^* \approx 0.765$), the upper edge of the band gap, ω_{up}^2, should be of the order of

$$\omega_f^2 = \mathscr{K}^* \Big/ M^* \approx 8.3. \tag{13}$$

and its width $\Delta\omega^2 \approx 2$ (see. Eq. (10)) that is in good agreement with the data shown in Fig. 5(d). However, the edges of the band gap, ω_{down}^2 and ω_{up}^2, which are visible in Fig. 5(d), are noticeably shifted down about half of the width, $\Delta\omega^2$ ($\Delta\omega^2/2 \approx 1$) relative to the frequencies ω_0^2 and ω_f^2, respectively. With increasing elasticity parameters, η and χ, the band gap moves upwards without noticeable changes in its width, while frequencies ω_{down}^2 and ω_{up}^2 approach their limit values of ω_0^2 and ω_f^2 ($\omega_{down}^2 \approx 5.97$ and $\omega_{up}^2 \approx 8.01$ at $\eta = \chi = 2$).

To establish the driving physical factors of such dynamics, let us analyze the types of modes that are responsible for the subsequent band gap dynamics (Figs. 5(e) and (f)). Naturally, the spatial structure of the 3D-oscillation modes excited in AMMs is very diverse. But at the singular points (see Fig. 4) of the Brillouin zone, similar to the one-dimensional case considered above, all oscillation modes can be divided into two groups - symmetric (at the equivalent lattice points of the metamaterial, the displacements are equal and in phase) and antisymmetric (at the equivalent lattice points of the metamaterial, the displacements are in antiphase). The type of symmetry is determined by the coordinates $\widehat{k}_x, \widehat{k}_y, \widehat{k}_z$ ($\widehat{k}_{x,y,z} = 0,\ \pm\pi$) of the singular point and the corresponding sign of the Bloch factor $\nu = \exp[i(\widehat{k}_x + \widehat{k}_y + \widehat{k}_z)] = \pm 1$. The degree of sensitivity of such modes to changes in the elasticity of the environment and the shell corresponds quite well to the results of the one-dimensional case considered above (Fig. 2B), which is easy to see in the data presented in Fig. 5.

The lower edge of the bandgap, ω_{down}^2, in all configurations shown in Fig. 5 is defined by an asymmetric ($\nu = -1$) oscillation mode

at point X of the Brillouin zone, $\omega^2_{(X)down}$, which refers to one of the mode sets either $\{A_s\}$ or $\{A_a\}$. Recall that the modes of the sets $\{A_s\}$ or $\{A_a\}$ respond only to changes in either the stiffness of the external environment or to changes in the stiffness of the shell (see Fig. 2B), respectively. It is easy to establish that the analyzed mode belongs to the set $\{A_s\}$. Indeed, the frequency $\omega^2_{(X)down}$ does not respond to changes in the stiffness, η, of the internal springs of the shell – the values of this frequency in Figs. 5(d) and 5(c) are practically unchanged, although the value η in the latter case is three times lower. In addition, the values of $\omega^2_{(X)down}$ in Figs. 5(f) and 5 (b), where the stiffness values η also differ by a factor of three for the fixed values of χ, are visually equal. At the same time, the frequency $\omega^2_{(X)down}$ and as a consequence its associated mode, are sensitive to variations in the elasticity of the environment, χ. This is easy to see when comparing the values of $\omega^2_{(X)down}$ in the data pair in Figs. 5(b) and 5(d) and the data pair of Figs. 5(c) and 5(f) at constant values of η in each of the variants. This fact can be easily explained qualitatively. At point X ($\widehat{k}_x = \pi$ and $\widehat{k}_y = \widehat{k}_z = 0$), the cores of neighboring cells oscillate in antiphase ($\nu = -1$) relative to each other along x-axis, compressing/stretching the space between the corresponding deforming shells. The increasing stiffness of this space, χ, makes the walls of the shells immobile, and $\omega^2_{(X)down}$ tends to ω^2_0.

The frequencies, $\omega^2_{(M_{1,2})acoust}$, at points M_1 and M_2 ($\nu = 1$) on the acoustic branches of oscillations increase with the stiffness χ similarly to frequency $\omega^2_{(X)down}$. However, at these points the displacements of the particles are transverse to the direction of wave propagation (orthogonal polarization or transverse waves). The shells of the unit cells also become immobile at high stiffness values χ, but the effect of 'freezing' of their mobility at shear strains of the environment between neighboring cells is weaker, and $\omega^2_{(M_{1,2})acoust} < \omega^2_{(X)down}$.

Prior to the formation of the band gap, the upper acoustic branch of oscillations and the lower optical branch form a conical intersection of two energy surfaces [86] in the vicinity of singular points of the Brillouin zone (one such intersection is marked in Fig. 5 (f) by arrows), which splits into two states as the rigidity of the acoustic system's skeleton increases. After this splitting, the upper frequencies of the type $\widehat{\omega}^2_{(X)}$ and $\widehat{\omega}^2_{(M)}$ are not bounded by the condition of in-phase displacement of the core and shell. The frequencies, $\widehat{\omega}^2_{(X)}(\eta,\chi)$ and $\widehat{\omega}^2_{(M)}(\eta,\chi)$, respond differently to changes in the values of stiffness parameters η and χ, but are similar in that they increase indefinitely with increasing η and χ, and each can determine the upper edge of the formed band gap, ω^2_{up} (see Fig. 5(b) - $\omega^2_{up} = \widehat{\omega}^2_{(M_1)}(\eta,\chi)$; 5(c) - $\omega^2_{up} = \widehat{\omega}^2_{(X)}(\eta,\chi)$; 5(e) - $\omega^2_{up} \approx \widehat{\omega}^2_{(X)}(\eta,\chi) \approx \widehat{\omega}^2_{(M_1)}(\eta,\chi)$). The accompanying widening of the band gap occurs rather abruptly until ω^2_{up} equals the lowest frequency of optical vibrations, $\omega^2_{(\Gamma)}$. If we track the development of the band gap from the configuration shown in Fig. 5(f) to the configuration of Fig. 5(d) then the frequency $\omega^2_{(\Gamma)}(\chi,\eta)$ becomes the upper edge of the band gap at $\chi = \eta = 0.55$ ($\omega^2_{(\Gamma),up}(\chi,\eta) = 7.05$, $\Delta\omega^2 = 2.08$).

To the frequency of oscillations, $\omega^2_{(\Gamma)}$, there corresponds a mode of the S_s – type, in which the vibrations of the cores and shells are antiphase to each other in each unit cell, but these vibrations are in phase in neighboring unit cells. In the one-dimensional acoustic chain, that mode is insensitive to variations in χ and η, as in this case the shell (particles A and B in Fig. 2B) moves as a whole. In a 3D metamaterial with a flexible shell, the frequency $\omega^2_{(\Gamma)}$ nevertheless responds to changes in the stiffness of both the shell and the environment, and is almost equally affected by them, which can be seen by comparing the data presented in Fig. 5(d) with the data in Figs. 5(b) and (c). However, once the frequency $\omega^2_{(\Gamma)}$ becomes the upper edge of the band gap, $\omega^2_{(\Gamma)up}$ at a sufficiently high value of χ, further growth of $\omega^2_{(\Gamma)up}$ (and the band gap width, $\Delta\omega^2$, accordingly) turns significantly less sensitive to changes in environmental/skeleton rigidity as the shells of the unit cells become gradually 'frozen'.

Only at high values of η and χ does the shape of the shell become 'frozen' (where the displacements of the shell particles are almost the same) and the frequency $\omega^2_{(\Gamma),up}$ rises to its limit given in Eq. (13) while the frequency $\omega^2_{(M)}(\chi,\eta)$ increases indefinitely. If the initial stiffness parameters of the medium and shells assume sufficiently high values, then such a slow transitional evolution to the stationary state is feasible as was observed in several previous investigations [75,85].

4.2. Controllable set of band gaps in metamaterials with multi-particle cores

In the cases of AMM's studied below, the core itself possesses many modes of oscillation even in the presence of a stationary shell. If the shell is elastic, then to some extent it mimics the non-local interaction between the particles of the core, causing the interaction between the vibrations of its individual parts. This interaction depends on the stiffness of the shell, which determines the length of the waves excited on its surface and their frequency. At high values of η, the metamaterial has a fixed set of band gaps independent of the stiffness χ [31] since the unit cells turn into simple mass-in-mass multi-resonators. Moderate values of η provide the connection between the surface waves of neighboring shells and, accordingly, the impact of the external medium on the vibrations of the cores. It is under such circumstances that it is possible to effectively control the set of band gaps formed by changing the rigidity of the external environment.

The data presented in Fig. 6 confirm the qualitative analysis above of the general acoustic properties of the metamaterials considered. At a relatively low stiffness of external springs, χ, the line frequency spectrum of isolated unit cells splits into many pass bands separated by band gaps (Fig. 6A). Increasing the stiffness of the environment, χ, increases the coupling between the surface modes of neighboring shells and the vibrational modes of neighboring cores. The corresponding splitting of the energy levels leads to

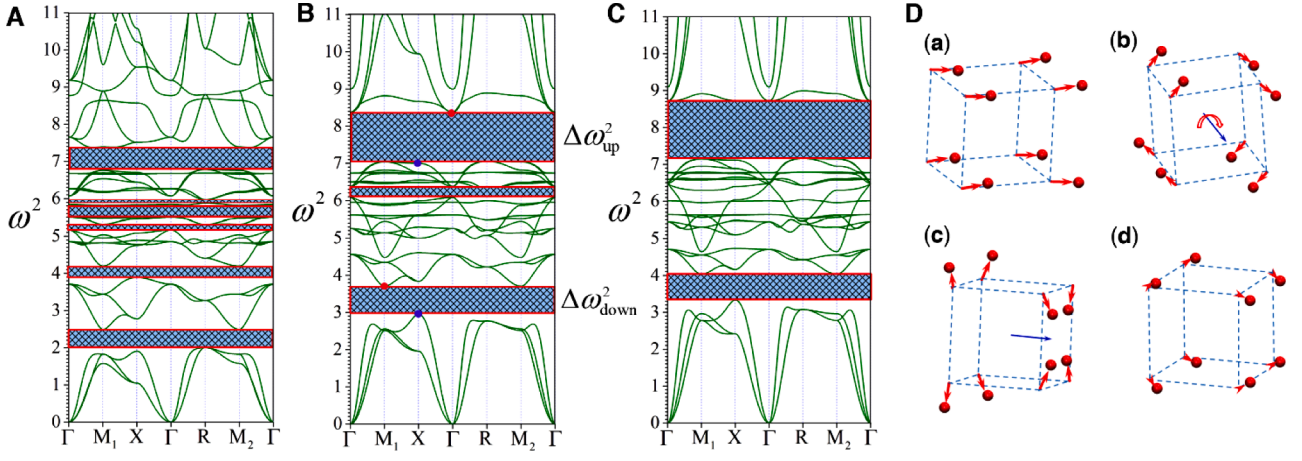

Fig. 6. Dynamics of the band gap set at a fixed shell stiffness $\eta = 1.5$, $N_{core} = 2^3$, $N_{shell} = 56$, and $m_{shell} = 0.125$ (core mass $M_{core} = 8$ and shell mass $M_{shell} = 7$). In subparts (**A**), (**B**), and (**C**) the stiffness of the outer springs, χ, is 0.25, 0.75, and 1.25 respectively. (**D**) Displacements of core particles in different vibrational modes at singular points of the Brillouin zone marked in subpart B by blue and red dots. Configurations (**a**) and (**c**) correspond to the lower edges of the lower and upper band gaps, respectively. In both cases, the amplitude of longitudinal displacements of core particles (in configuration (c) along the blue axis) is strictly the same. Configuration (**b**) represents the rotational oscillations of the core at point M_1 - the upper edge of the lower band gap. Displacements of core particles along the axis of rotation are equal to zero. Configuration (**d**) represents displacements of core particles in the uppermost band gap edge (point Γ). The displacements of the 56 shell particles are not shown to facilitate a visual representation of the morphology of the fundamental vibration modes.

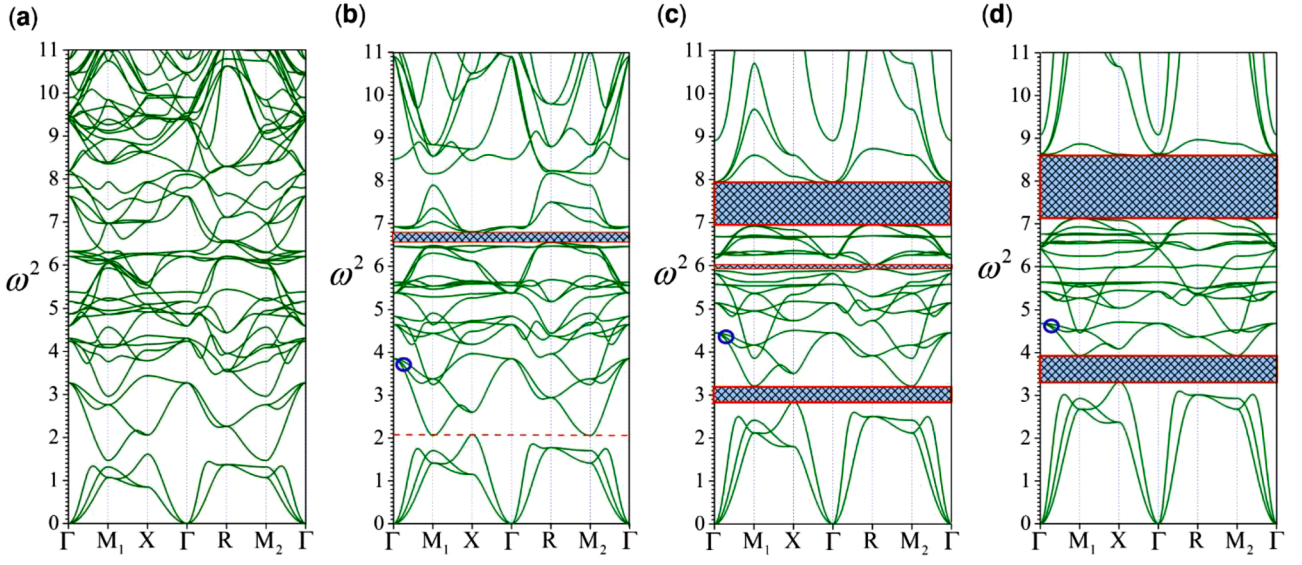

Fig. 7. Dynamics of the band gap set with variation in the stiffness of a homogeneous medium surrounding the cores of unit cells of the metamaterial, $N_{core} = 2^3, N_{shell} = 56, \eta = \chi$; $m_{shell} = 0.125, M_{core} = 8$, and $M_{shell} = 7$. In configurations (**a**) to (**d**), the stiffness of the external and shell springs is 0.25, 0.38, 0.75, and 1.25, respectively.

the overlap of adjacent passbands and the disappearance of single band gaps (Fig. 6C). Note that the formation of the edges of the most stable lower and upper band gaps quite fully corresponds to the classical physical mechanisms—in-phase vibrations of the core and shell at the lower edge of the band gap and their antiphase vibrations at the upper edge of the band gap.

Based on the concepts above, the characteristic frequency of the lower bandgap with the width $\Delta\omega^2_{down}$ (see Fig. 6B) can be estimated as the oscillation frequency of the core relative to the fixed shell. If we consider all the external bonds of the particles of the core according to Eq. (9), the sets of which are equivalent for each of the N_{core} core particles in the case under consideration, then the calculation of the force, F_{core}, acting by the low displacement of the core as a whole, Δ_{core}, leads to the relation:

$$F_{core} \approx -N_{core} \cdot 4.47 \cdot \Delta_{core}. \tag{14}$$

Thus, the frequency range of the lower bandgap should be close to the estimation $\Omega^2_{low} = F_{core}/M_{core} \approx 4.47$ ($M_{core} = N_{core} \cdot m = N_{core}$), which corresponds quite well to the data presented in Figs. 6B and C. In addition, at the edges of the lower bandgap, $\Delta\omega^2_{down}$, the motion of the cores as single entities is indeed realized–see Fig. 6D, configurations (a) and (b). However, on its upper edge, instead of antiphase vibrational oscillations of the cores and shells, rotational oscillations are excited. The singular point M of the Brillouin zone corresponds to symmetric oscillation modes, $\nu = \exp[i(\widehat{k}_x + \widehat{k}_y + \widehat{k}_z)] = 1$, i.e., all cores rotate in phase relative to each other but in antiphase relative to the rotation of the surrounding shells.

An estimate of the characteristic frequency, Ω^2_{upper}, of the uppermost bandgap with a width of $\Delta\omega^2_{up}$ is given by the oscillation frequency of a single particle in the core. If neighboring particles are stationary, then such a frequency, according to expression (12), is approximately 6.4. Taking into account the antiphase displacement of particles in the cores (see Fig. 6D, configuration (c)) it was possible to foresee the results observed in Figs. 6B and C – characteristic frequencies of the upper band gap, Ω^2_{upper}, lie above 6.4. At the lower edge of the upper band gap, $\Delta\omega^2_{up}$, displacements of the cores as a whole are also realized up to some extent (see Fig. 6D(c)), however, the amplitude of oscillations of the particles of the cores along the blue axis is much smaller than the amplitude of their oscillations in the transverse direction. It is the transverse antiphase oscillations that determine the frequency at the lower edge of the band gap. The higher frequency at its upper edge ($\widehat{k} = 0$) at relatively small displacements of the core particles (see Fig. 6D(d)) is due to more significant antiphase displacements of the shells relative to the cores.

One can see that the state of the acoustic system, shown in Fig. 6B, is close to stationary. An increase in environmental rigidity, χ, by a factor of ~1.7 (see Figs. 6B and 6C) slightly changes the position and width of the main band gaps, $\Delta\omega^2_{down}(\eta,\chi)$ and $\Delta\omega^2_{up}(\eta,\chi)$.

The results of Fig. 6 were obtained with a sufficiently high value of fixed shell stiffness, η. Band gap control modes with varying rigidity of the homogeneous medium surrounding the cores, $\eta = \chi$, are preferable, a fact which is demonstrated by the results shown in Fig. 7. In the quasi-saturation mode, the parameters of the formed band gaps (see Figs. 7(c) and 7(d)) are practically the same as before (see Fig. 6C), but with a decrease in the rigidity of the environment through alteration in magnetic field induction, it is possible to transform the band gaps into pass bands (see Fig. 7(a)) since in the low-frequency range the density of skeleton states increases.

Results presented in Fig. 7(b) can be explained based on different qualitative models. The focus here, however, is on the band gap formation model discussed above. At the upper edge of the formed band gap, an antiphase oscillation mode of the core and shell always appears. For a relatively flexible shell i.e. if the rigidity of the shell is insufficient, then the excitation of such a mode is difficult, especially at low frequencies and, accordingly, long-wavelength surface vibration modes of the shell. At high frequencies (short-wavelength surface modes), the local curvature of the shell surface increases, and the corresponding 'surface pressure' increases which can provide antiphase oscillations with short-scale oscillations of the cores. It is with this effect that the earlier formation of the upper band gap, $\Delta\omega^2_{up}$, is observed in Fig. 7(b).

As noted above, as the stiffness of the external environment increases, the dynamics of the set of band gaps approach a quasi-stationary regime (see Figs. 6B, 6C and 7(c), 7(d)). It is important to note that the emergence of a quasi-stationary mode is in itself rather peculiar in metamaterials with multi-particle cores. As one can see in Figs. 6B, 6C and 7(c), 7(d), the lower edge, $\omega^2_{down(\min)}(\chi,\eta)$, of the lowest band gap is very close to the oscillation frequency, ω^2_0, ($\omega^2_0 = 4.47$ according to Eq. (12)) and the upper edge, $\omega^2_{up(\max)}(\chi,\eta)$, of the uppermost band gap is bounded from above by the frequency ω^2_f, which is also easily calculated from Eq. (13) as:

$$\omega^2_f = N_{core} \cdot 4.47 \Big/ M^* \approx 9.6, \tag{15}$$

where the reduced mass is $M^* = M_{core}M_{shell}/(M_{core} + M_{shell}) \approx 3.73$ ($M_{core} = 8$ and $M_{shell} = 7$).

Thus, if the unit cells were simple mass-in-mass vibrators, the band gap formed would correspond to the frequency range $\omega^2_0 \le \omega^2 \le \omega^2_f$. However, in the case under consideration, this range is rather wide and includes a series of intermediate frequency branches (see Figs. 6C and 7(d)), which are formed as a consequence of coupling between the natural vibrations of cores and shells. As the stiffness of the skeleton ($\eta = \chi$) increases, the characteristic frequencies of the shell vibrations increase and their coupling with the lower-frequency vibrations of the core is weakened. This effect is noticeable in Figs. 7(b), (c), and (d) in which the group of frequency branches marked by the blue ring, to take as an example, gradually narrow down with increasing stiffnesses η and χ. A pictorial consequence of the increase in these parameters is shown in Fig. 8A where the narrowing of the intermediate frequency branches resulted in a set of new band gaps.

Thus, in the case of the multi-particle cores, the frequency interval

$$\omega^2_0 \le \omega^2 \le \omega^2_f, \tag{16}$$

gives a reasonable estimate of the limits of the so-called 'band gaps creation region', within which both the formation of a dense set of band gaps at large skeleton stiffness (see Fig. 8A) and the full opening of this range for acoustic waves at lower skeleton stiffness are possible (see Fig. 7(a)).

Note that the frequency, ω_f^2, depends on the reduced mass of the unit cell. At the fixed core mass the reduced mass increases with increasing the shell mass. This dependence makes it possible to reduce the upper limit of the upper band gap when increasing the shell mass and achieve the formation of only a controlled low-frequency band gap above the acoustic branches of the dispersion relation (see Figs. 8B and C).

A remarkable fact is that changing the shell mass does not change the value of $\omega^2_{down(\min)}(\chi,\eta)$ (see Figs. 8A and C), which, once again, confirms this fundamental characteristic of the band gaps creation region. The correctness of the qualitative analysis above is also confirmed by the data presented in Fig. 9 with a higher number of masses in the multi-particle unit cell core ($N_{core} = 3^3$). An increase in the stiffness of the environment enhances the coupling between the shortwave/high-frequency modes of the shells and cores. The band gaps formed subsequently are gradually shifted to the high-frequency region of the spectrum (see Fig. 9(b),(c),(d)). An estimate of the oscillation frequency of the core, ω_0^2, with a stationary shell gives the value $\omega_0^2 \sim 3.32$. The upper limit of the band gaps creation region, ω_f^2, at given core and shell masses of $M_{core} = 27$ and $M_{shell} = 12.25$ is equal to 10.63. Thus, the formation of band gaps is expected to arise within the frequency range of $3.32 \leq \omega^2 \leq 10.63$, which is in good agreement with the data shown in Fig. 9. It is in the proximity of frequency ω_0^2 that a low-frequency band gap should form, however, with a many-particle heavy core immersed in a soft shell, the coupling between their low-frequency modes is weak. As a result, even with a high stiffness of the environment, when the upper band gap has just formed, the low-frequency band gap is in its 'infancy' (Fig. 9(d)) and appears only at $\eta = \chi \gtrsim 1.5$.

Instead of increasing the ambient stiffness to form a low-frequency band gap, a simpler method exists to achieve this goal. It is sufficient, for example, to replace the central particle of the core with a particle of a larger mass. Then, on the one hand, for the same number of core's eigenmodes, the low-frequency region of the spectrum will be filled more densely, which will provide effective coupling of the vibrational modes of the core and the shell and on the other hand, the high-frequency vibrations of the core will be mainly due to the surface motion of particles along its faces and edges. Under these circumstances, the formation of a low-frequency bandgap will not significantly affect the dynamics of high-frequency band gaps as the two mechanisms correspond to different positional allocations for vibrational modes in space. This qualitative analysis of the consequences of the proposed modification in the core structure/mass is consistent with the data presented in Fig. 10.

The results shown in Figs. 9 and 10 are suggestive of using multilayered cores instead of a simple increase in the number of particles of uniform mass in it. A multi-layered core with an inhomogeneous distribution of particle masses is an open-type multivibrator with a flexible shell. An example of a unit cell with such a multilayered core is shown in Fig. 11(a). The dynamics of the band gaps of the corresponding 3D-metamaterial with variations in the elasticity of the external medium ($\eta = \chi$) are shown in Figs. 11(b), (c), and (d).

The unit cell presented in Fig. 11(a) is an analog of a mass-in-mass type multivibrator that has four nested elements: a central heavy particle of mass $m_c = 5$, a shell of 26 magenta particles surrounding it with the mass of $m_{mag} = 3$ each, and the next layer which is a

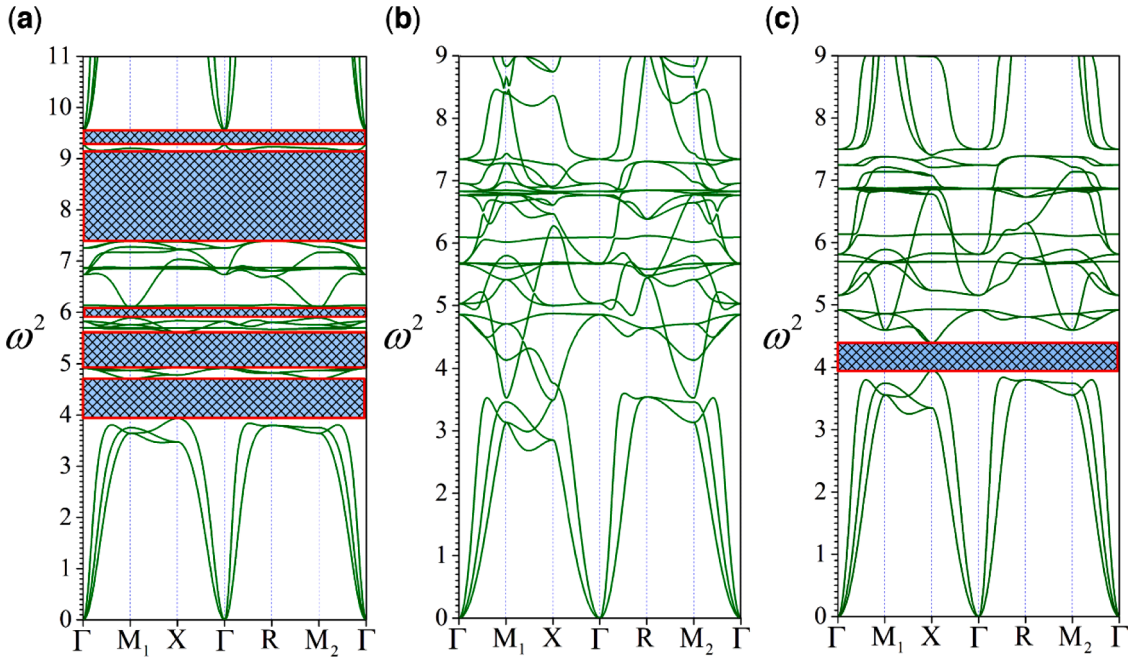

Fig. 8. Examples of varying degrees of filling the band gaps creation area. (**a**) $\eta = \chi = 4$, and the rest of the parameters are the same as in Fig. 7. (**b**) & (**c**) $N_{core} = 2^3, N_{shell} = 56, m_{shell} = 0.5, M_{core} = 8$, and $M_{shell} = 28$. The stiffnesses are $\eta = \chi = 3$ and 4.6, respectively.

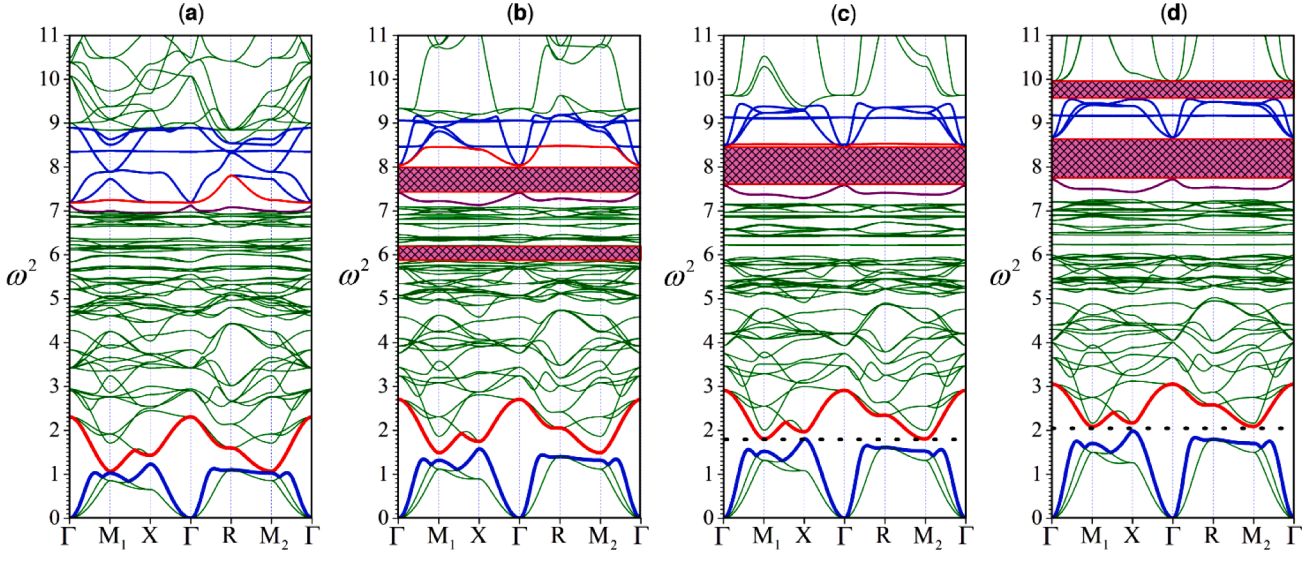

Fig. 9. Dynamics of the band gap set of a metamaterial with the number of particles in the core $N_{core} = 3^3$, $N_{shell} = 98$. The stiffness of the medium surrounding the cores of elementary cells is homogeneous: $\eta = \chi$ and $m_{shell} = 0.125$ ($M_{core} = 27$ and $M_{shell} = 12.25$). In configurations (**a**) to (**d**), the external and shell stiffnesses are 0.40, 0.65, 0.90, and 1.20, respectively. Band gaps in the range $\omega^2 > 3$ with a width, $\Delta\omega^2$, less than 0.3 are not highlighted.

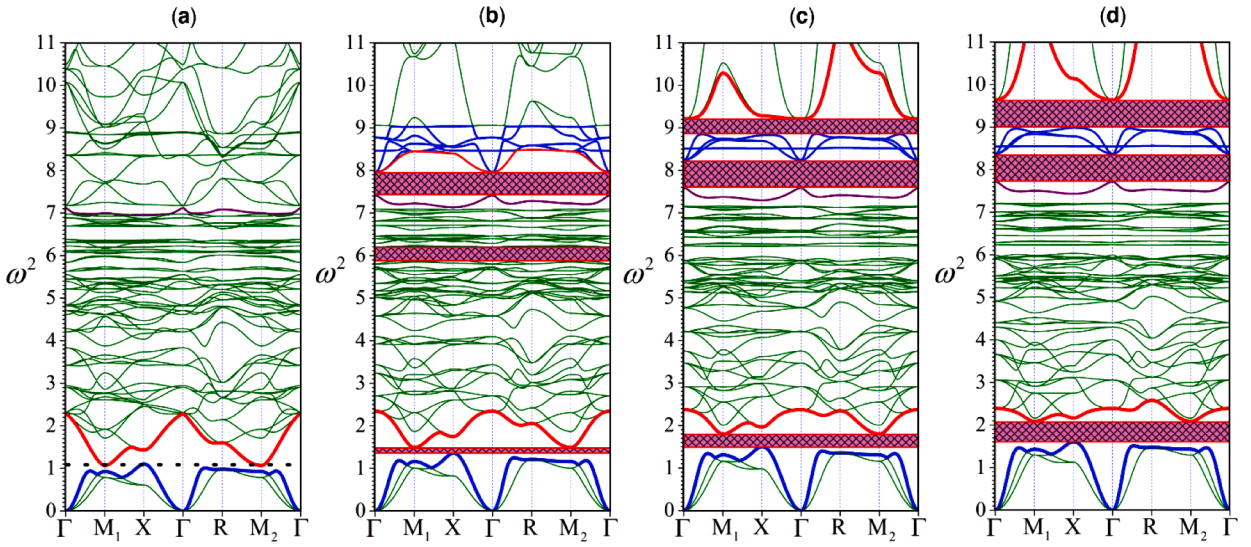

Fig. 10. Dynamics of the band gap set of a metamaterial with the number of particles in the core $N_{core} = 3^3$. The stiffness of the medium surrounding the cores of elementary cells is homogeneous: $\eta = \chi$ and $m_{shell} = 0.125$. The mass of the central particle, m_c, in the core has been increased to 2.4. In configurations (**a**) to (**d**), the external and shell stiffnesses are 0.40, 0.65, 0.90, and 1.20, respectively. Band gaps in the range $\omega^2 > 3$ with a width, $\Delta\omega^2$, less than 0.3 are not highlighted.

shell of 98 red particles with the mass of $m = 1$ each. The super-core is enclosed by the outermost shell (marked by a blue color), which simultaneously represents the external environment. The stiffness of the springs, κ, connecting concurrently the elements of the super-core to one another and the outer shell is assumed to be equal, as before, to unity, $\kappa = 1$.

A classic multivibrator with four nested masses has three non-zero eigenfrequencies. Accordingly, in an external field, the acoustic environment built from these multivibrators would form three band gaps [31] with edges that do not depend on the stiffness of the external environment. Thus, in the metamaterial with the super unit cells shown in Fig. 11(a), it is indeed possible to form three band gaps, as shown in Figs. 11(b-d), but both the number of gaps formed and their upper/lower edges are functions of the stiffnesses χ and η (see Figs. 11(b),(c), and (d)). The detailed band gap dynamics of this case is shown in the video file 'Super-Core_dyncs.mp4' (see Supplementary materials).

4.3. *Controlled directional transmissibility of acoustic waves in anisotropic metamaterials*

In two-dimensional structures, the formation of directional band gaps (prohibiting propagation of acoustic waves within specified frequency ranges and along prescribed directions) was considered in several previous works [87–89]. To achieve directional broadband gaps for flexural waves at mid-to-low frequencies, researchers [88] have proposed a kind of periodic plate carved inside with tunneled acoustic black holes that generate band gaps through locally resonant effects of the created cells. Another proposed 2D model of a phononic crystal [89], is a periodic structure made of rectangular unit super-cells that consist of 25 conventional rectangular unit cells. Below, we show the possibility of creating a 3D-metamaterial based on primitive cells with a relatively simple topology and morphology (see Fig. 12), which implements controlled dynamics of both full and directional band gaps.

The methodology for constructing the dispersion relations (equations of motion for unit cell particles) is the same as that used above (see Section 3). The only distinctive feature to be taken into account is the anisotropy (in this case orthotropy) meaning that the integral acoustic structure formed has different period of translational symmetry, $\mathscr{L}$, along different coordinate axes: $\mathscr{L}_x = \mathscr{L}_y = 3$, and $\mathscr{L}_z = 5$. Accordingly, the components of the dimensionless wave vector are equal to $\widehat{k}_x = 2\pi\mathscr{L}_x/\lambda$, $\widehat{k}_y = 2\pi\mathscr{L}_y/\lambda$, and $\widehat{k}_z = 2\pi\mathscr{L}_z/\lambda$. Considering the special type of anisotropy in the acoustic properties of the metamaterial, the calculation of frequency branches, $\omega^2 = \omega_n^2(\boldsymbol{k})$, presented in Fig. 13 is conducted along the trajectory in the first Brillouin zone shown in Fig. 12(b). It was assumed that the constitutive relations associated with the elastic medium surrounding the cores of the unit cells are those of homogeneous materials ($\eta = \chi$).

The sequence of states of the acoustic metamaterial, shown in Fig. 13 can be easily interpreted qualitatively. The three-particle core of the unit cell shown in Fig. 12(a) is an open-type multivibrator because each of the core particles interacts with the environment. Nevertheless, the formation of the two full bandgaps is consistent with physical concepts developed for metamaterials, in which the core of the unit cell is a multivibrator with a mass-in-mass structure [31] and eigenfrequencies of the multivibrator with fixed outer shell signify the lower edges of the formed bandgaps. In the case under consideration, the set of these eigenfrequencies, $\{\Omega_0^2\}$, includes only three values, which we show below.

All degenerate modes of the horizontal vibrations of particles of the core have the same frequency, $\omega_{0,hor}^2$, which is equal to the

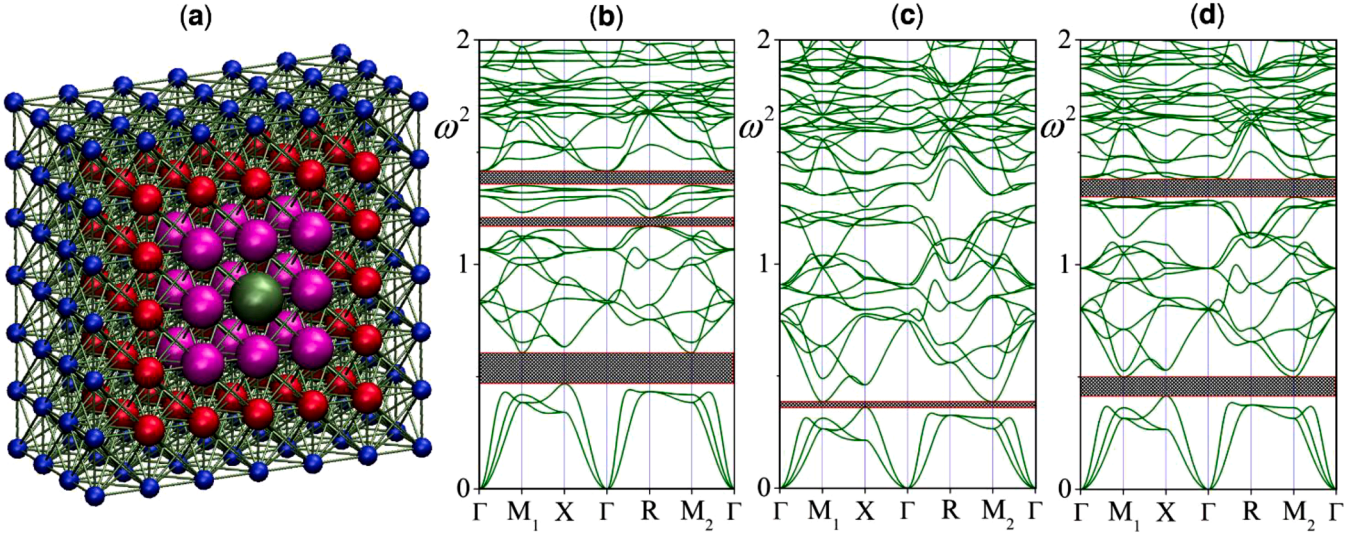

Fig. 11. Dynamics of band gaps in a metamaterial with inhomogeneous super-cores in unit cells. Configuration (**a**) is the central section of the multilayer unit cell. The mass of the central olive particle $m_c = 5$, the mass of magenta particles surrounding it $m_{mag} = 3$, the mass of red particles $m = 1$, the mass of the blue particles $m_{shell} = 0.25$. The stiffness, κ, of the springs connecting the particles of the super-core to one another and with the outer blue shell is equal to one, $\kappa = 1$. Configurations (**b**), (**c**), and (**d**) represent the frequency branches, $\omega^2 = \omega_n^2(\hat{k})$, of the metamaterial for different values of the rigidity of the medium surrounding the core: $\eta = \chi = 0.6,\ 1.0,$ and 2.0, respectively.

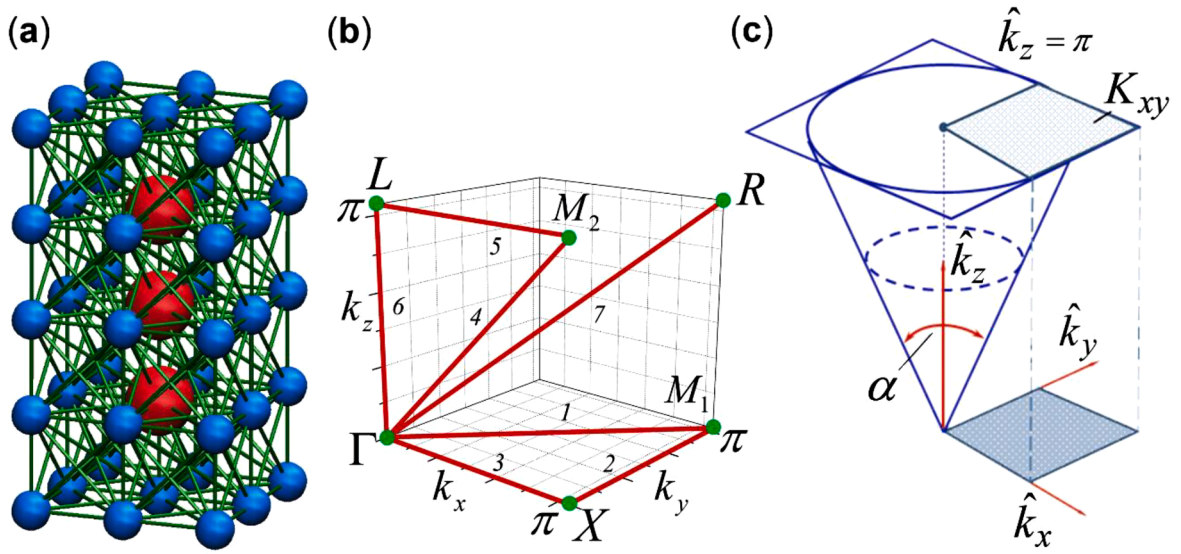

Fig. 12. Spring-mass model of an anisotropic acoustic metamaterial. (**a**) The unit cell of the metamaterial. (**b**) Trajectory in the first Brillouin zone along which the frequency branches, $\omega^2 = \omega_n^2(\hat{\boldsymbol{k}})$, are calculated. (**c**) A conical region in $\hat{\boldsymbol{k}}$-space, in which the passage of acoustic waves is studied and the corresponding spectral diagram is plotted.

frequency of oscillations of the single-particle core, ω_0^2, under the action of 26 springs (see Eq. (12)), since at their small horizontal displacements (as shown in Fig. 14(a)) the local interaction of the neighboring particles (among themselves) does not appear:

$$\omega_{0,hor}^2 = \omega_0^2 = \mathscr{K}^* \Big/ m_{core} \approx 6.37 \tag{17}$$

Among the three possible vertical vibrations of the core, one of the modes where the central particle of the core stands still, and the opposite ends oscillate in antiphase relative to each other, also has the frequency ω_0^2. The frequencies of the other two modescan be easily calculated based on the equations of motion (9) for three core particles. Thus the complete set of eigenfrequencies, $\{\Omega_0^2\}$ is of the form:

$$\{\Omega_0^2\} = \begin{cases} \omega_{0,ver2}^2 \approx \omega_0^2 + \sqrt{2} \approx 7.78 \\ \omega_0^2 \approx 6.37 \ (degenerate\ energy\ level) \\ \omega_{0,ver1}^2 \approx \omega_0^2 - \sqrt{2} \approx 4.96 \end{cases} \tag{18}$$

It is therefore clear that the coupling between the oscillation modes of cores and shells, which increases with the increase in the stiffness of the environment, leads to the formation of three directional band gaps (Fig. 13(b)) in the proximity of frequencies $\{\Omega_0^2\}$ (for waves propagating along the axis of the core - $\Gamma - L$ path section in Fig. 12(b)). With a further increase in the value of elasticity parameter χ, the two lower directional band gaps successively transform into two full bandgaps (see Figs. 13(c) and (d)). Note that despite the multitude of particles in the shells of the unit cells, they are indeed practically immobile at the lower edges of the bandgaps, $\omega_{down,1}^2$ and $\omega_{down,2}^2$, (see Figs. 14(a) and (b)), and shift as a whole at their upper edges, $\omega_{up,1}^2$ and $\omega_{up,2}^2$ (see Fig. 14(c) and (d)) at large values of stiffness of the environment. Accordingly, the frequencies $\omega_{up,1}^2$ and $\omega_{up,2}^2$ can be estimated quite accurately when calculating the eigenfrequencies of a generalized system of four interacting particles moving along the unit cell axis (the Z axis in Fig. 12). The number of eigenfrequencies different from 0 in such a problem, as in the problem with a stationary shell (see Eq. (18)), equals 3, but in both cases, only the modes in which the central particle of the core moves in antiphase relative to the other two (see Fig. 14) determine the edges of the formed bandgaps in the quasi-stationary regime.

In contrast to full bandgaps, whose parameters change slightly with variations in the rigidity of the medium/shell, the edges of the directional bandgap, $\omega_{dir,down}^2$ and $\omega_{dir,up}^2$, shift significantly with different mobility, which results in noticeable changes in the width of this band gap, $\Delta\omega_{dir}^2$. It can be seen that the value of $\Delta\omega_{dir}^2$ first increases (see Figs. 13(b) and (c)), and then decreases to zero – see Figs. 13(c), (d), and (e). The different dynamics of the edges of the directional bandgap are due to differences in the morphology of vibrational modes (see Fig. 15) that define its lower and upper edges. It is the specificity of deformations of the unit cell shell and the environment that determines the different degree of response of the values $\omega_{dir,down}^2(\eta,\chi)$, and $\omega_{dir,up}^2(\eta,\chi)$ to changes in the stiffnesses η and χ. For example, the shell stiffness, η, is a more significant factor in the longitudinal vibrations of the unit cell (see Fig. 15(a)) than in its transverse/flexural vibrations at the upper edge of the directional bandgap - see Fig. 15(b), which is reflected in the results of Figs. 13(d) and (e). With a simultaneous increase in stiffness parameters η and χ ($\eta = \chi > 0.75$), the mobility of frequency $\omega_{dir,down}^2(\eta,\chi)$

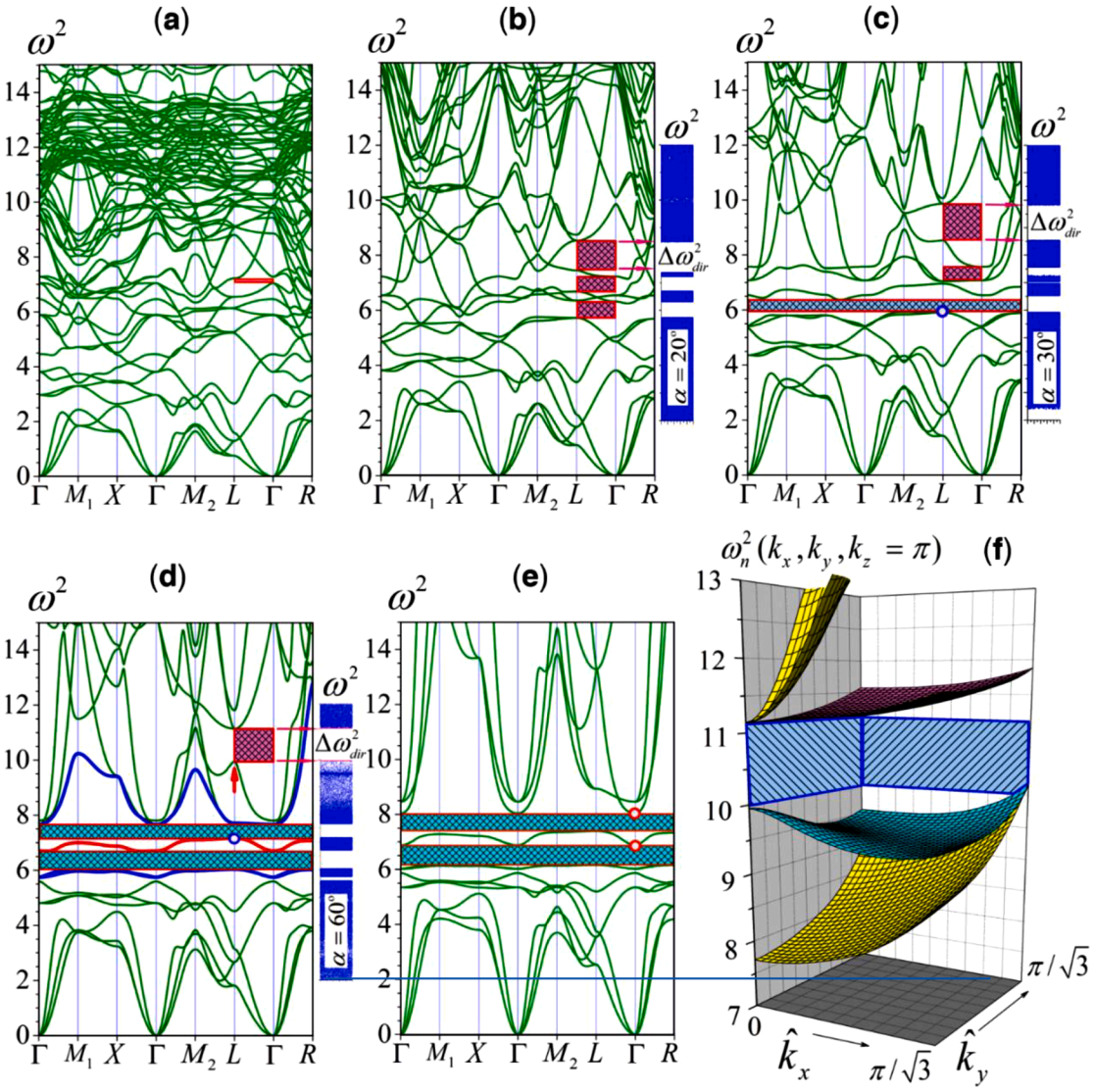

Fig. 13. Dynamics of the set of band gaps in the studied anisotropic material – see Fig. 12. The rigidity of the medium surrounding the cores of elementary cells k is homogeneous: $\eta = \chi$; the mass of shell particles $m_{shell} = 0.125$. In configurations (**a**) to (**e**), the external and shell stiffnesses are 0.25, 0.40, 0.55, 0.75, and 1.2, respectively. The eigenvectors for the upper and lower edges of the band gaps (marked respectively by blue and red rings in configurations (c), (d), and (e)) are shown in Fig. 14. Configuration (**f**) represents the frequency surfaces, $\omega^2 = \omega_n^2(\boldsymbol{k})$, adjacent to the directionally oriented band gap, $\Delta\omega^2_{dir}$, observed in configuration (d) – magenta colored rectangle.

is more pronounced than the mobility of frequency $\omega^2_{dir,up}(\eta,\chi)$, which causes narrowing the width of the directional bandgap, $\Delta\omega^2_{dir}$, down to zero, essentially closing it. If the data in Fig. 13(d) take as some initial state and at the fixed value of $\eta = 0.75$ an increase only of the stiffness parameter χ to 1.2, then the increase in frequency $\omega^2_{dir,down}(\eta,\chi)$ lags behind the increasing value of $\omega^2_{dir,up}(\eta,\chi)$, and the directional bandgap does not disappear as it has occurred in Fig. 13(e) ($\eta = \chi = 1.2$). Moreover, its width, $\Delta\omega^2_{dir}$, becomes 0.26 larger relative to the data shown in Fig. 13(d) even when shifting up the lower edge, $\omega^2_{dir,down}$, by one.

Note that in addition to the width of the directional bandgap, $\Delta\omega^2_{dir}$, the bandgap possesses another important physical characteristic worth being mentioned viz. the angle of the band gap cone, α (see Fig. 12(c)). The frequency band $\Delta\omega^2_{dir}$ is guaranteed to be prohibited for waves propagating strictly along the *Z*-axis ($\hat{k}_x = \hat{k}_y = 0$ and $0 \le \hat{k}_z \le \pi$). However, the band gap of the same width is also formed for a certain set of waves (a set of wave vectors $\{\hat{\boldsymbol{k}}\}$) propagating at some angles, β, relative to this axis, $\beta \le \alpha/2$. The set $\{\hat{\boldsymbol{k}}\}$ fills some cone with the angle at its vertex, α, in the first Brillouin zone. To determine the value of this angle, the following procedure may be performed. In an arbitrary cone in the $\hat{\boldsymbol{k}}$–space (see Fig. 12(c)), a large number (in this case 10,000) of points were randomly selected, for which all eigenfrequencies of the system were calculated. The set of all these frequencies forms a spectral

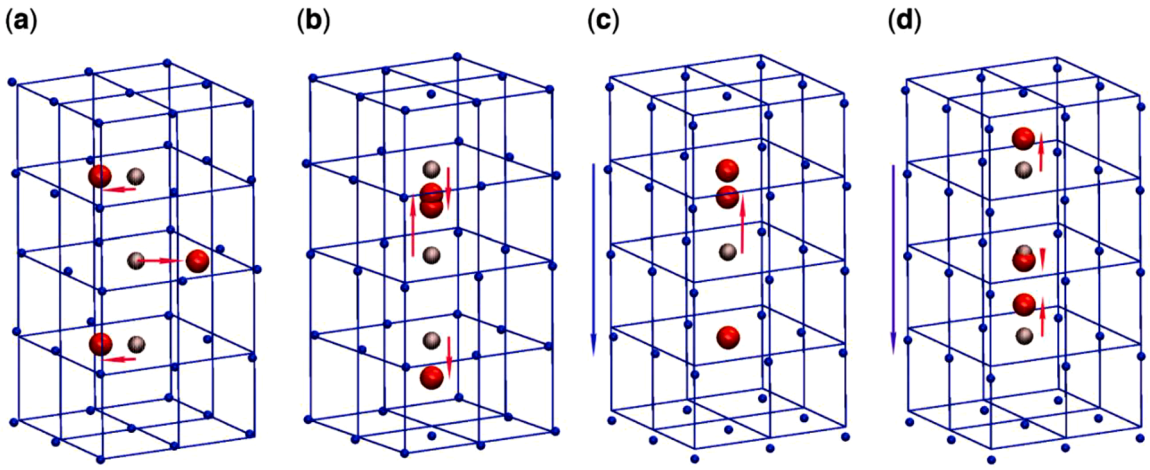

Fig. 14. Eigenvectors of particle displacements of the unit cell for vibration modes which represent the lower and upper edges of the band gaps in the configurations of Figs. 13(c), (d), and (e), where they are marked with blue and red rings, respectively. The initial positions of the shell particles coincide with the nodes of the cubic lattice (blue lines). The blue dots show the localization of the displaced shell particles. The initial and final positions of the core particles are represented by gray and red spheres, respectively. Configurations (**a**) and (**b**) correspond to the lower edges of band gaps (see Figs. 13(c) and (d)). The morphologies of these modes depict vibrations of type A_s (see Fig. 2B). Configurations (**c**) and (**d**) correspond to the upper edges of band gaps (see Fig. 13(e)). These oscillation modes are of the S_s type (see Fig. 2B).

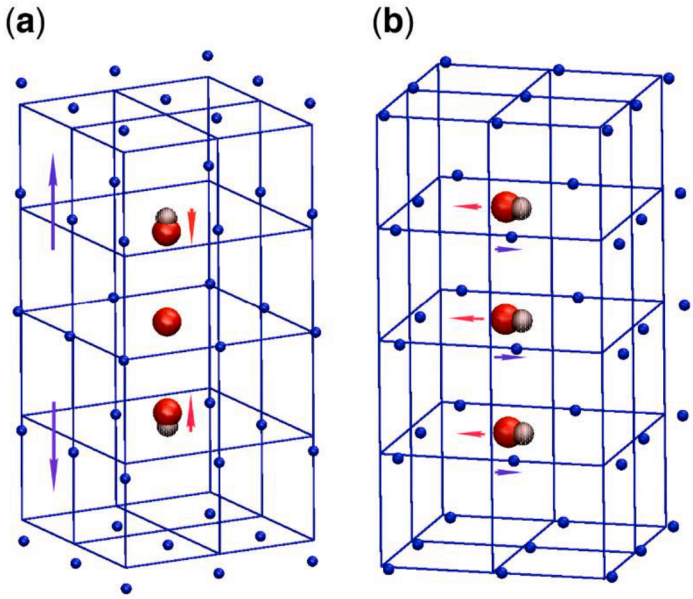

Fig. 15. Eigenvectors of unit cell particle displacements for vibration modes that determine the (**a**) lower and (**b**) upper edge of the directionally oriented band gap (see the red arrow in Fig. 13(d)).

diagram (see vertical blue stripes in Fig. 13), which displays all band gaps for the selected set of wave vectors. The angle at the vertex of the cone, α, was fitted such that the highest frequency gap in the spectral diagram was equal to $\Delta\omega^2_{dir}$.

From the comparison of the data presented in Figs. 13(b), (c), and (d), it can be deduced that the dynamics of the band gap, $\Delta\omega^2_{dir}$, with varying stiffness parameters η and χ, differs from the dynamics of the 'angular width', α, and the narrowing of the band gap on the frequency axis can be accompanied by the extension of band gap cone in the $\widehat{\boldsymbol{k}}$- space.

Thus, when designing metamaterials with different levels of response sensitivity in elasticity parameters, $\eta(B)$ and $\chi(B)$, to changes in the norm of induction of an external magnetic field, $\boldsymbol{B}$, various scenarios can be implemented to control the characteristics of the directional band gap in almost real-time. The details were discussed in the present work and many aspects of the smart controllable behavior were quantified.

5. Conclusions

This work deals with the formation of smart controllable bandgaps governed by real-time sensitivity of elastic constitutive parameters to an external magnetic field induction. The detailed qualitative and quantitative analyses of a diversity of scenarios for the dynamics of generated bandgaps in an alternating magnetic field, which we carried out in this work, lays the ground and provides basic concepts for optimizing the parameters of specific acoustic 3D systems of given dynamic parameters for a particular response.

The dominating physical factor that determines the features of investigated dynamic processes is the tunable elasticity of the shells of unit cells and their ability to generate surface vibrational modes. The formation of discontinuities in a primary dense spectrum of frequencies, $\Omega^2 = \{0 \le \omega^2 \le \omega^2_{max}\}$ that corresponds to the set of dispersion-surfaces, $\{\omega^2_n(\widehat{\boldsymbol{k}},\eta,\chi)\}$, of the entire acoustic system is based on the inhomogeneity of the shifts, $\Delta\omega^2_n(\widehat{\boldsymbol{k}},\eta,\chi)$, of the frequency surfaces, $\{\omega^2_n(\widehat{\boldsymbol{k}},\eta,\chi)\}$, along the frequency axis when variating the stiffnesses $\eta(B)$ and $\chi(B)$:

$$\Delta\omega^2_n(\widehat{\boldsymbol{k}},\eta,\chi) = \left[\partial\omega^2_n(\widehat{\boldsymbol{k}},\eta,\chi) \,/\, \partial\chi\right]\Delta\chi + \left[\partial\omega^2_n(\widehat{\boldsymbol{k}},\eta,\chi) \,/\, \partial\eta\right]\Delta\eta \equiv \beta^{(\chi)}_{n,\widehat{\boldsymbol{k}}}\Delta\chi + \beta^{(\eta)}_{n,\widehat{\boldsymbol{k}}}\Delta\eta.$$

The heterogeneity of the 'mobilities' $\beta^{(\chi)}_{n,\widehat{\boldsymbol{k}}}$ and $\beta^{(\eta)}_{n,\widehat{\boldsymbol{k}}}$ with respect to mode number n, is associated with different levels of coupling between the vibration modes of the unit cell cores and the external simply-connected medium (the metamaterial skeleton).

The evolution of band gaps formed by increasing stiffnesses η and χ occurs in three stages: dynamic, quasi-stationary, and overcritical. The features of each stage are as follows:

I. In the one-dimensional metamaterial with nonlocal interactions, there are four types of modes of oscillation, which respond differently to changes in the values of $\eta(B)$ and $\chi(B)$ at singular points of the Brillouin zone. In a three-dimensional metamaterial with elastic shells of unit cells, similar features appear at sufficiently high stiffness of the skeleton, when the corresponding wavelengths for low-frequency surface modes gradually increase and the displacements of the shell particles become homogeneous up to a large extent. In this stage, i.e., the 'dynamic' stage, the band gaps arise due to the significant heterogeneity of the mobilities $\beta^{(\chi)}_{n,\widehat{\boldsymbol{k}}}$ and $\beta^{(\eta)}_{n,\widehat{\boldsymbol{k}}}$ with respect to mode number, n, and splitting the frequency surfaces at the vicinity of their conical intersection. As the intensity of the magnetic field (skeleton stiffness) increases, the band gaps expand quite sharply due to the withdrawal of the more mobile frequency surfaces from the so-called 'band gaps creation region'. At this stage, the number of band gaps can also significantly change.

II. In the quasi-stationary stage, the edges of the band gaps are represented only by slow frequency surfaces (with low values of $\beta^{(\chi)}_{n,\widehat{\boldsymbol{k}}}$ and $\beta^{(\eta)}_{n,\widehat{\boldsymbol{k}}}$) since the fastest modes have left the 'band gaps creation region'. In the modes of oscillations that fill the band gaps creation region, the displacements of the shell particles become increasingly homogeneous. Accordingly, the edges of the formed band gaps slowly approach their limits as the displacements of the shells relative to each other 'freeze' as the skeleton stiffness increases. The transmission ranges between band gaps are filled with *intermediate* optical frequency surfaces, $\overline{\overline{\omega}}^2_{m(opt)}(\widehat{\boldsymbol{k}},\eta,\chi)$, which also practically do not shift along the frequency axis.

III. At very high values of skeleton stiffness, some of the intermediate frequency surfaces, $\overline{\overline{\omega}}^2_{m(opt)}(\widehat{\boldsymbol{k}},\eta,\chi)$, degenerate into planes with frequencies of natural vibrations of the multiparticle cores enclosed in the stationary shells. In this supercritical stage, the number of band gaps in the 'band gaps creation region' can start to increase again, as seen in Fig. 8A.

In anisotropic structures with a wide variety of nondegenerate frequency/energy surfaces, simultaneous generation of both full and directional band gaps is possible. The controllable parameters of such band gaps are their frequency and angular widths. It is therefore possible to achieve full control through the alteration of system parameters affecting the angular width and frequency ranges of the gaps.

CRediT authorship contribution statement

V.N. Gorshkov: Conceptualization, Methodology, Analyses **V.O. Kolupaiev**: Programming, Data generation, Writing- Original draft preparation. **N. Mehreganian**: Programming, Visualization, Investigation. **G.K. Boiger**: Supervision, Writing- Reviewing and Editing, **P. Sareh:** Analyses, Validation, Figures: **A. S. Fallah: Methodology, Analyses,** Writing- Reviewing and Editing

Declaration of Competing Interest

The authors declare that they have no known competing financial interests or personal relationships that could have appeared to influence the work reported in this paper.

Data availability

The authors confirm that the data supporting the findings of this study are available within the article.

Acknowledgment

The research presented in this paper was supported by the Swiss National Science Foundation (SNSF) under the Scientific Exchanges' Mobility Grant (Grant No.: IZSEZ0_206111).

Supplementary materials

Supplementary material associated with this article can be found, in the online version, at doi:10.1016/j.jsv.2023.118157.

References

[1] A.S. Fallah, Y. Yang, R. Ward, M. Tootkaboni, R. Brambleby, A. Louhghalam, et al., Wave propagation in two-dimensional anisotropic acoustic metamaterials of K4 topology, Wave Motion 58 (2015) 101–116, https://doi.org/10.1016/j.wavemoti.2015.07.001.
[2] V.N. Gorshkov, N. Navadeh, A.S. Fallah, A study of frequency band structure in two-dimensional homogeneous anisotropic phononic K3-metamaterials, Smart Mater. Struct. 26 (2017), 095058, https://doi.org/10.1088/1361-665x/aa7dfa.
[3] H.H. Huang, C.T. Sun, G.L. Huang, On the negative effective mass density in acoustic metamaterials, Int. J. Eng. Sci. 47 (2009) 610–617, https://doi.org/10.1016/j.ijengsci.2008.12.007.
[4] B. Sharma, C.T. Sun, Local resonance and Bragg bandgaps in Sandwich beams containing periodically inserted resonators, J. Sound Vib. 364 (2016) 133–146, https://doi.org/10.1016/j.jsv.2015.11.019.
[5] S. Zhang, D.A. Genov, C. Sun, X. Zhang, Cloaking of matter waves, Phys. Rev. Lett. 100 (2008), https://doi.org/10.1103/physrevlett.100.123002.
[6] W. Cai, V. Shalaev, Optical Metamaterials Fundamentals and Applications, Springer New York, New York, NY, 2010.
[7] R. Fleury, A. Alù, Extraordinary sound transmission through density-near-zero ultranarrow channels, Phys. Rev. Lett. 111 (2013), https://doi.org/10.1103/physrevlett.111.055501.
[8] D.R. Smith, J.B. Pendry, M.C. Wiltshire, Metamaterials and negative refractive index, Science 305 (2004) 788–792, https://doi.org/10.1126/science.1096796.
[9] Y.C. Wang, R.S. Lakes, Extreme stiffness systems due to negative stiffness elements, Am. J. Phys. 72 (1) (2004) 40–50.
[10] N. Mehreganian, A.S. Fallah, P. Sareh, Structural mechanics of negative stiffness honeycomb metamaterials, J. Appl. Mech. 88 (5) (2021) 051006.
[11] N. Mehreganian, A.S. Fallah, P. Sareh, Impact response of negative stiffness curved-beam-architected metastructures, Int. J. Solids Struct. (2023) 112389.
[12] B.M. Goldsberry, M.R. Haberman, Negative stiffness honeycombs as tunable elastic metamaterials, J. Appl. Phys. 123 (9) (2018).
[13] E. Jalali, H. Soltanizadeh, Y. Chen, Y.M. Xie, P. Sareh, Selective hinge removal strategy for architecting hierarchical auxetic metamaterials, Commun. Mater. 3 (1) (2022) 97.
[14] H.M. Kolken, A.A. Zadpoor, Auxetic mechanical metamaterials, RSC Adv. 7 (9) (2017) 5111–5129.
[15] J.K. Wilt, C. Yang, G.X. Gu, Accelerating auxetic metamaterial design with deep learning, Adv. Eng. Mater. 22 (5) (2020) 1901266.
[16] Y. Chen, W. Ye, R. Xu, Y. Sun, J. Feng, P. Sareh, A programmable auxetic metamaterial with tunable crystal symmetry, Int. J. Mech. Sci. 249 (2023) 108249.
[17] S. Zhang, C. Xia, N. Fang, Broadband acoustic cloak for ultrasound waves, Phys. Rev. Lett. 106 (2011), https://doi.org/10.1103/physrevlett.106.024301.
[18] S.A. Cummer, J. Christensen, A. Alù, Controlling sound with acoustic metamaterials, Nat. Rev. Mater. 1 (2016), https://doi.org/10.1038/natrevmats.2016.1.
[19] J. Li, L. Fok, X. Yin, G. Bartal, X. Zhang, Experimental demonstration of an acoustic magnifying hyperlens, Nat. Mater. 8 (2009) 931–934, https://doi.org/10.1038/nmat2561.
[20] L. Zigoneanu, B.I. Popa, S.A. Cummer, Design and measurements of a broadband two-dimensional acoustic lens, Phys. Rev. B 84 (2011), https://doi.org/10.1103/physrevb.84.024305.
[21] C. Cai, Z. Wang, Y. Chu, G. Liu, Z. Xu, The phononic band gaps of Bragg scattering and locally resonant pentamode metamaterials, J. Phys. D 50 (2017), 415105, https://doi.org/10.1088/1361-6463/aa83ec.
[22] T. Lee, H. Iizuka, Bragg scattering based acoustic topological transition controlled by local resonance, Phys. Rev. B 99 (2019), https://doi.org/10.1103/physrevb.99.064305.
[23] Y. Xiao, J. Wen, G. Wang, X. Wen, Theoretical and experimental study of locally resonant and Bragg band gaps in flexural beams carrying periodic arrays of beam-like resonators, J. Vib. Acoust. 135 (2013), https://doi.org/10.1115/1.4024214.
[24] A.O. Krushynska, M. Miniaci, F. Bosia, N.M. Pugno, Coupling local resonance with Bragg band gaps in single-phase mechanical metamaterials, Extreme Mech. Lett. 12 (2017) 30–36, https://doi.org/10.1016/j.eml.2016.10.004.
[25] M. Cenedese, E. Belloni, F. Braghin, Interaction of Bragg scattering bandgaps and local resonators in mono-coupled periodic structures, J. Appl. Phys. 129 (2021), 124501, https://doi.org/10.1063/5.0038438.
[26] N. Fang, D. Xi, J. Xu, M. Ambati, W. Srituravanich, C. Sun, et al., Ultrasonic metamaterials with negative modulus, Nat. Mater. 5 (2006) 452–456, https://doi.org/10.1038/nmat1644.
[27] W.N. Yunker, C.B. Stevens, G.T. Flowers, R.N. Dean, Sound attenuation using microelectromechanical systems fabricated acoustic metamaterials, J. Appl. Phys. 113 (2013), 024906, https://doi.org/10.1063/1.4774021.
[28] X. Jiang, Y. Li, B. Liang, Jian-chun Cheng, L. Zhang, Convert acoustic resonances to orbital angular momentum, Phys. Rev. Lett. 117 (2016), https://doi.org/10.1103/physrevlett.117.034301.
[29] X. Chen, X. Xu, S. Ai, H.S. Chen, Y. Pei, X. Zhou, Active acoustic metamaterials with tunable effective mass density by gradient magnetic fields, Appl. Phys. Lett. 105 (2014), 071913, https://doi.org/10.1063/1.4893921.
[30] X. Wang, X. Luo, H. Zhao, Z. Huang, Acoustic perfect absorption and broadband insulation achieved by double-zero metamaterials, Appl. Phys. Lett. 112 (2018), 021901, https://doi.org/10.1063/1.5018180.
[31] V. Gorshkov, P. Sareh, N. Navadeh, V. Tereshchuk, A.S. Fallah, Multi-resonator metamaterials as multi-band metastructures, Mater. Des. 202 (2021), 109522, https://doi.org/10.1016/j.matdes.2021.109522.
[32] G.L. Huang, C.T. Sun, Band gaps in a multiresonator acoustic metamaterial, J. Vib. Acoust. 132 (2010), https://doi.org/10.1115/1.4000784.
[33] A.S. Fallah, N. Navadeh, V.V. Tereshchuk, V.N. Gorshkov, Phononic dispersion in anisotropic pseudo-fractal hyper-lattices, Mater. Des. 164 (2019), 107560, https://doi.org/10.1016/j.matdes.2018.107560.
[34] X. Man, Z. Luo, J. Liu, B. Xia, Hilbert fractal acoustic metamaterials with negative mass density and bulk modulus on subwavelength scale, Mater. Des. 180 (2019), 107911, https://doi.org/10.1016/j.matdes.2019.107911.
[35] K. Wang, Y. Liu, T. Liang, Band structures in Sierpinski triangle fractal porous phononic crystals, Phys. B 498 (2016) 33–42, https://doi.org/10.1016/j.physb.2016.06.018.
[36] A. Bacigalupo, L. Gambarotta, Simplified modelling of chiral lattice materials with local resonators, Int. J. Solids Struct. 83 (2016) 126–141, https://doi.org/10.1016/j.ijsolstr.2016.01.005.
[37] S. Jin, Y.P. Korkolis, Y. Li, Shear resistance of an auxetic chiral mechanical metamaterial, Int. J. Solids Struct. 174-175 (2019) 28–37, https://doi.org/10.1016/j.ijsolstr.2019.06.005.

[38] A.O. Krushynska, F. Bosia, M. Miniaci, N.M. Pugno, Spider web-structured labyrinthine acoustic metamaterials for low-frequency sound control, New J. Phys. 19 (2017), 105001, https://doi.org/10.1088/1367-2630/aa83f3.
[39] T. Frenzel, J.D. Brehm, T. Bückmann, R. Schittny, M. Kadic, M. Wegener, Three-dimensional labyrinthine acoustic metamaterials, Appl. Phys. Lett. 103 (2013), 061907, https://doi.org/10.1063/1.4817934.
[40] C. Liu, B. Xia, D. Yu, The spiral-labyrinthine acoustic metamaterial by coiling up space, Phys. Lett. A 381 (2017) 3112–3118, https://doi.org/10.1016/j.physleta.2017.07.041.
[41] R. Ghaffarivardavagh, J. Nikolajczyk, S. Anderson, X. Zhang, Ultra-open acoustic metamaterial silencer based on Fano-like interference, Phys. Rev. B 99 (2019), https://doi.org/10.1103/physrevb.99.024302.
[42] J. Han, S. Tang, R. Wang, W. Wang, Acoustic wave transmission channel based on phononic crystal line defect state, AIP Adv. 9 (2019), 065201, https://doi.org/10.1063/1.5098819.
[43] C. Shen, Y. Xie, N. Sui, W. Wang, S.A. Cummer, Y. Jing, Broadband acoustic hyperbolic metamaterial, Phys. Rev. Lett. 115 (2015), https://doi.org/10.1103/physrevlett.115.254301.
[44] A. Climente, D. Torrent, J. Sánchez-Dehesa, Omnidirectional broadband insulating device for flexural waves in thin plates, J. Appl. Phys. 114 (2013), 214903, https://doi.org/10.1063/1.4839375.
[45] M. Farhat, S. Enoch, S. Guenneau, A.B. Movchan, Broadband cylindrical acoustic cloak for linear surface waves in a fluid, Phys. Rev. Lett. 101 (2008), https://doi.org/10.1103/physrevlett.101.134501.
[46] R. Liu, C. Ji, J.J. Mock, J.Y. Chin, T.J. Cui, D.R. Smith, Broadband ground-plane cloak, Science 323 (2009) 366–369, https://doi.org/10.1126/science.1166949.
[47] B. Xia, N. Chen, L. Xie, Y. Qin, D. Yu, Temperature-controlled tunable acoustic metamaterial with active band gap and negative bulk modulus, Appl. Acoust. 112 (2016) 1–9, https://doi.org/10.1016/j.apacoust.2016.05.005.
[48] M. Maldovan, Phonon wave interference and thermal bandgap materials, Nat. Mater. 14 (2015) 667–674, https://doi.org/10.1038/nmat4308.
[49] S. Sepehri, M.M. Mashhadi, M.M. Seyyed Fakhrabadi, Active/passive tuning of wave propagation in phononic microbeams via piezoelectric patches, Mech. Mater. 167 (2022), 104249, https://doi.org/10.1016/j.mechmat.2022.104249.
[50] K. Miura, Map fold a la Miura style, its physical characteristics and application to the space science, Res. Pattern Form. (1994) 77–90.
[51] P. Sareh, The least symmetric crystallographic derivative of the developable double corrugation surface: Computational design using underlying conic and cubic curves, Mater. Des. 183 (2019) 108128.
[52] Y. Nishiyama, Miura folding: Applying origami to space exploration, Int. J. Pure Appl. Math. 79 (2) (2012) 269–279.
[53] X. Zhang, X. Huang, G. Lu, Tunable bandgaps and acoustic characteristics of perforated Miura-ori phononic structures, Int. J. Mech. Sci. 253 (2023), 108389, https://doi.org/10.1016/j.ijmecsci.2023.108389.
[54] X. Lu, X. Wu, H. Xiang, J. Shen, Y. Li, Y. Li, et al., Triple tunability of phononic bandgaps for three-dimensional printed hollow sphere lattice metamaterials, Int. J. Mech. Sci. 221 (2022), 107166, https://doi.org/10.1016/j.ijmecsci.2022.107166.
[55] W.H. Li, X.Z. Zhang, H. Du, Magnetorheological elastomers and their applications, Adv. Struct. Mater. (2013) 357–374, https://doi.org/10.1007/978-3-642-20925-3_12.
[56] W. Wang, Y.Q. Guo, W.Q. Chen, Effect of negative permeability on elastic wave propagation in magnetoelastic multilayered composites, Theor. Appl. Mech. Lett. 7 (2017) 126–133, https://doi.org/10.1016/j.taml.2017.01.006.
[57] A. Dargahi, R. Sedaghati, S. Rakheja, On the properties of magnetorheological elastomers in shear mode: design, fabrication and characterization, Compos. B 159 (2019) 269–283, https://doi.org/10.1016/j.compositesb.2018.09.080.
[58] K. Nagashima, T. Mitsumata, Magnetorheological effect for bimodal magnetic elastomers, Int. Polym. Sci. Technol. 44 (2017) 45–50, https://doi.org/10.1177/0307174x1704400607.
[59] D. Borin, G. Stepanov, A. Musikhin, A. Zubarev, A. Bakhtiiarov, P. Storozhenko, Magnetorheological effect of magnetoactive elastomer with a permalloy filler, Polymers 12 (2020) 2371, https://doi.org/10.3390/polym12102371.
[60] J.M. Linke, D.Y. Borin, S. Odenbach, First-order reversal curve analysis of magnetoactive elastomers, RSC Adv. 6 (2016) 100407–100416, https://doi.org/10.1039/c6ra23435f.
[61] H. Böse, R. Röder, Magnetorheological elastomers with high variability of their mechanical properties, J. Phys. Conf. Ser. 149 (2009), 012090, https://doi.org/10.1088/1742-6596/149/1/012090.
[62] T. Mitsumata, S. Ohori, Magnetic polyurethane elastomers with wide range modulation of elasticity, Polym. Chem. 2 (2011) 1063–1067, https://doi.org/10.1039/c1py00033k.
[63] T. Mitsumata, S. Ohori, A. Honda, M. Kawai, Magnetism and viscoelasticity of magnetic elastomers with wide range modulation of dynamic modulus, Soft Matter 9 (2013) 904–912, https://doi.org/10.1039/c2sm26717a.
[64] M. Kukla, Ł. Warguła, K. Talaśka, D. Wojtkowiak, Magnetorheological elastomer stress relaxation behaviour during compression: experiment and modelling, Materials 13 (2020) 4795, https://doi.org/10.3390/ma13214795.
[65] S. Samal, M. Škodová, L. Abate, I. Blanco, Magneto-rheological elastomer composites. A review, Appl. Sci. 10 (2020) 4899, https://doi.org/10.3390/app10144899.
[66] T. Li, A. Abd El-Aty, C. Cheng, Y. Shen, C. Wu, Q. Yang, et al., Investigate the effect of the magnetic field on the mechanical properties of silicone rubber-based anisotropic magnetorheological elastomer during curing process, J. Renew. Mater. 8 (2020) 1411–1427, https://doi.org/10.32604/jrm.2020.012939.
[67] S. Kashima, F. Miyasaka, K. Hirata, Novel soft actuator using magnetorheological elastomer, IEEE Trans. Magn. 48 (2012) 1649–1652, https://doi.org/10.1109/tmag.2011.2173669.
[68] H. Du, W. Li, N. Zhang, Semi-active variable stiffness vibration control of vehicle seat suspension using an mr elastomer isolator, Smart Mater. Struct. 20 (2011), 105003, https://doi.org/10.1088/0964-1726/20/10/105003.
[69] S. Qi, H. Guo, J. Chen, J. Fu, C. Hu, M. Yu, et al., Magnetorheological elastomers enabled high-sensitive self-powered tribo-sensor for Magnetic Field Detection, Nanoscale 10 (2018) 4745–4752, https://doi.org/10.1039/c7nr09129j.
[70] T. Hu, S. Xuan, L. Ding, X. Gong, Stretchable and Magneto-sensitive strain sensor based on silver nanowire-polyurethane sponge enhanced magnetorheological elastomer, Mater. Des. 156 (2018) 528–537, https://doi.org/10.1016/j.matdes.2018.07.024.
[71] H. Böse, R. Rabindranath, J. Ehrlich, Soft magnetorheological elastomers as new actuators for valves, J. Intell. Mater. Syst. Struct. 23 (2012) 989–994, https://doi.org/10.1177/1045389x11433498.
[72] H.X. Deng, X.L. Gong, Application of magnetorheological elastomer to vibration absorber, Commun. Nonlinear Sci. Numer. Simul. 13 (2008) 1938–1947, https://doi.org/10.1016/j.cnsns.2007.03.024.
[73] H.K. Kim, H.S. Kim, Y.K. Kim, Stiffness control of magnetorheological gels for adaptive tunable vibration absorber, Smart Mater. Struct. 26 (2016), 015016, https://doi.org/10.1088/1361-665x/26/1/015016.
[74] Y. Li, J. Li, T. Tian, W. Li, A highly adjustable magnetorheological elastomer base isolator for applications of real-time adaptive control, Smart Mater. Struct. 22 (2013), 095020, https://doi.org/10.1088/0964-1726/22/9/095020.
[75] W. Yan, G. Zhang, Y. Gao, Investigation on the tunability of the band structure of two-dimensional magnetorheological elastomers phononic crystals plate, J. Magn. Magn. Mater. 544 (2022), 168704, https://doi.org/10.1016/j.jmmm.2021.168704.
[76] G.J. Yu, X.X. Wen, C.B. Du, L.Y. Wang, S.J. Zhu, Study on bandgap vibration isolation of super-cell phononic crystals based on magnetorheological elastomers, AIP Adv. 11 (2021), 125113, https://doi.org/10.1063/5.0065140.
[77] K.H. Lee, K. Yu, H. Al Ba'ba'a, A. Xin, Z. Feng, Q. Wang, Sharkskin-inspired magnetoactive reconfigurable acoustic metamaterials, Research 2020 (2020), https://doi.org/10.34133/2020/4825185.
[78] C.D. Pierce, C.L. Willey, V.W. Chen, J.O. Hardin, J.D. Berrigan, A.T. Juhl, et al., Adaptive Elastic metastructures from Magneto-active elastomers, Smart Mater. Struct. 29 (2020), 065004, https://doi.org/10.1088/1361-665x/ab80e4.

[79] G. Zhang, Y. Gao, Tunability of band gaps in two-dimensional phononic crystals with magnetorheological and electrorheological composites, Acta Mech. Solida Sin. 34 (2020) 40–52, https://doi.org/10.1007/s10338-020-00189-6.
[80] B. Li, W. Yan, Y. Gao, Tunability of band gaps of programmable hard-magnetic soft material phononic crystals, Acta Mech. Solida Sin. 35 (2022) 719–732, https://doi.org/10.1007/s10338-022-00336-1.
[81] L. Wang, Z. Chen, L. Cheng, A metamaterial plate with magnetorheological elastomers and gradient resonators for tuneable, low-frequency and broadband flexural wave manipulation, Thin Walled Struct. 184 (2023), 110521, https://doi.org/10.1016/j.tws.2022.110521.
[82] Y. Wang, J. Yang, Z. Chen, Y. Lin, L. Gong, S. Zhang, et al., Investigation of a magnetorheological elastomer metamaterial sandwich beam with tunable graded stiffness for broadband vibration attenuation, Smart Mater. Struct. 32 (2023), 065022, https://doi.org/10.1088/1361-665x/acd289.
[83] N. Karami Mohammadi, P.I. Galich, A.O. Krushynska, S. Rudykh, Soft magnetoactive laminates: large deformations, transverse elastic waves and band gaps tunability by a magnetic field, J. Appl. Mech. 86 (2019), https://doi.org/10.1115/1.4044497.
[84] H. Jafari, R. Sedaghati, Analysis of an adaptive periodic low-frequency wave filter featuring magnetorheological elastomers, Polymers 15 (2023) 735, https://doi.org/10.3390/polym15030735.
[85] Z. Xu, J. Tong, F. Wu, Magnetorheological elastomer vibration isolation of tunable three-dimensional locally resonant acoustic metamaterial, Solid State Commun. 271 (2018) 51–55, https://doi.org/10.1016/j.ssc.2017.12.024.
[86] D.R. Yarkony, Diabolical conical intersections, Rev. Mod. Phys. 68 (1996) 985–1013, https://doi.org/10.1103/revmodphys.68.985.
[87] J. Li, S. Li, Z. Miao, Investigations on the complex band diagram of flexural wave through the fluid-loaded phononic plate, Appl. Sci. 12 (2022) 12386, https://doi.org/10.3390/app122312386.
[88] L. Tang, L. Cheng, Periodic plates with tunneled acoustic-black-holes for directional band gap generation, Mech. Syst. Signal Process. 133 (2019), 106257, https://doi.org/10.1016/j.ymssp.2019.106257.
[89] A. Singh, A. Gupta, Directional bandgap analysis in phononic crystal with rectangular super cell structure, Int. J. Math. Eng. Manag. Sci. 7 (2022) 341–349, https://doi.org/10.33889/ijmems.2022.7.3.023.